Supporting Information

Methanol Synthesis from CO_2/CO Mixture on Cu-Zn Catalyst from Microkinetics-Guided Machine Learning Pathway Search

Yun-Fei Shi[1], Pei-Lin Kang[1], Cheng Shang[1,2*], Zhi-Pan Liu[1,2,3*]

[1]Collaborative Innovation Center of Chemistry for Energy Material, Shanghai Key Laboratory of Molecular Catalysis and Innovative Materials, Key Laboratory of Computational Physical Science, Department of Chemistry, Fudan University, Shanghai 200433, China

[2]Shanghai Qi Zhi Institution, Shanghai 200030, China

[3]Key Laboratory of Synthetic and Self-Assembly Chemistry for Organic Functional Molecules, Shanghai Institute of Organic Chemistry, Chinese Academy of Sciences, Shanghai 200032, China

Corresponding Author: *cshang@fudan.edu.cn, *zpliu@fudan.edu.cn

Table of Contents

1 Microkinetics-Guided Machine Learning Pathway Search

In this section, we provide more details on the MMLPS method. We will first overview the SSW-RS method and then describe the parallel pathway sampling in the MMLPS method. The algorithms for reaction nominature in ECFP and the fast pathway filter are then followed.

1.1 SSW-RS

The SSW-RS method[1,2] is developed previously by our group to explore likely reactions for a given reactant. The method is modified upon the SSW global optimization method, where at the end of each step of SSW the occurrence of reaction is checked (e.g. by using the bond matrix of intermediates). If the reaction occurs in an SSW step, the initial minimum (initial state, IS) and the new minimum (final state, FS) are recorded as a reaction pair, and then SSW rejects the new minimum and continues. After certain steps of SSW with many reaction pairs collected, the double-ended surface walking (DESW)[3,4] method is utilized to search for the transition state (TS) of all collected IS/FS pairs. In short, SSW-RS samples the reactions with the same IS at different conformations, which provides the kinetics information on the lowest reaction channel leaving the current IS.

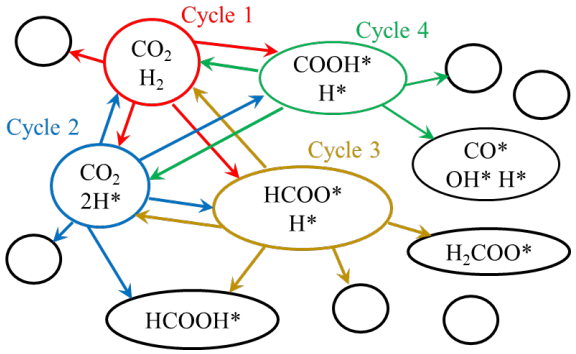

Figure S1. Snapshot for the first 4 cycles of on Cu(211) with starting molecules of CO_2+H_2. Circle represents intermediates, and arrow represents sampled reaction pairs from one intermediate to the other.

1.2 The parallel pathway sampling in the MMLPS method

An MMLPS simulation contains many branches running in parallel. In each branch, the chemical composition is fixed by the starting structure and will perform SSW-RS iteratively with each cycle starting from a different reactant.

To illustrate better how a single branch works, we take the CO_2+H_2 on Cu(211) as an example and the building of the reaction network by iterative SSW-RS is plotted in **Figure S1**. From CO_2 + H_2, the first cycle in SSW-RS obtains the low energy reaction pathways including H_2 → 2H* and H_2 + CO_2 → H* + HCOO*. Next, using the fast pathway filter as described below, the CO_2 + 2H* is selected as the new intermediate for the next SSW-RS cycle. In the second cycle, the low energy reactions including CO_2 + H* → HCOO*, 2H* → H_2, CO_2 + H* → COOH* are then discovered. Similarly, the HCOO*+H* is selected for the third cycle because of its lowest overall resistance from CO_2 + H_2. The COOH* + H* and the other higher energy pathways will also be selected subsequently to explore the reaction network in depth.

Obviously, the CO_2+H_2 (CO_2H_2 formula) branch cannot reach the target product, CH_3OH+H_2O (CO_2H_6 formula), and thus its reaction network is only a sub-network of methanol synthesis from CO_2 hydrogenation. The other branches of MMLPS, for example, starting from HCOOH+H_2 (CO_2H_4 composition) and HCHO+H_2 (COH_4

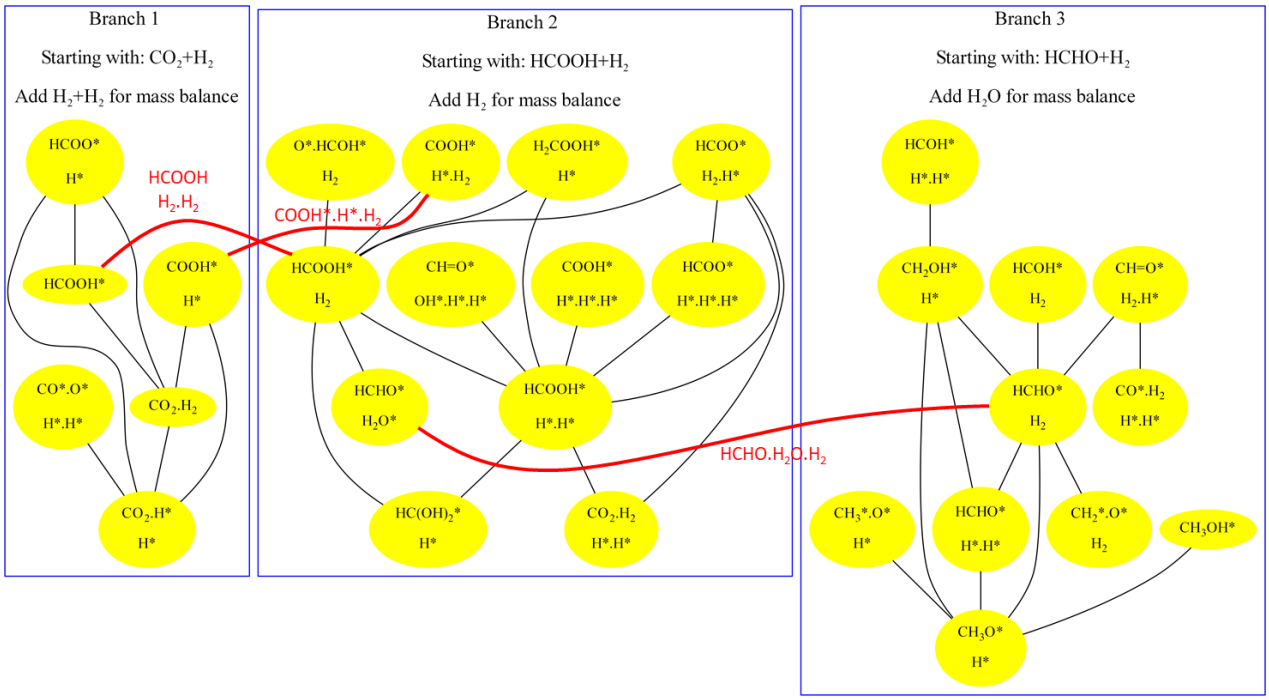

Figure S2. An example to merge three branches in MMLPS. The black line means the edge within the same branch, and the red line means that the nodes from different branches need to join together.

composition), that run in parallel, will produce the other necessary reaction pathways and by merging them together, the whole reaction network with the CO_2H_6 composition can be obtained.

In merging reactions from different branches, one needs to align the chemical composition to the same level. An example of how the reaction network (a graph with nodes) is merged is shown in **Figure S2**. The reactions in branch 1 that starts from CO_2+H_2, are amended with 2 virtual gas phase H_2 (e.g., the HCOOH* node is considered as HCOOH*+2H_2). Likely, the reactions in branch 2 that starts from HCOOH+H_2 are amended with 1 virtual gas phase H_2 (e.g., the HCHO*+H_2O* node is considered as HCHO*+H_2O*+H_2) and nodes in branch 3 are amended with 1 virtual gas phase H_2O. In practice, we add the name of virtual molecules to the chemical name of a node, (e.g., add "H2" to "COOH.H*" as "COOH.H*.H2"), which generates a mass-balanced chemical name. In the microkinetics analyzer submodule (see main text), the nodes that share the same mass-balanced chemical name (in different branches) will be merged into a single node with the appropriate Gibbs free energy correction so that different sub-networks are linked with each other. For example, HCHO*+H_2O* in branch 2 is in fact the same as HCHO*+H_2 in branch 3 with the same mass-balanced chemical name HCHO*+H_2O*+H_2. Note that the setting of starting molecules and the virtual molecules for each branch are manually designed as input for the MMLPS simulation.

1.3 Reaction nominature in ECFP

In the reaction pair database the reaction, as distinguishable by their IS and FS, is named by using ECFP method[5]. ECFP method gives a Hash value for a molecule from its bond matrix and elemental features, as already utilized in our previous work[6]. In this work, we only consider the bond matrix between C, H, and O elements, which means that the molecular adsorption, desorption diffusion, or surface reconstruction do not affect the ECFP name. The mapping between ECFP-4 name (ECFP at the level 4) and the chemical name can be manually established for quick reaction interpretation. An example of ECFP-4 name and chemical name is shown in **Figure S3**. Based on the ECFP-4 name,

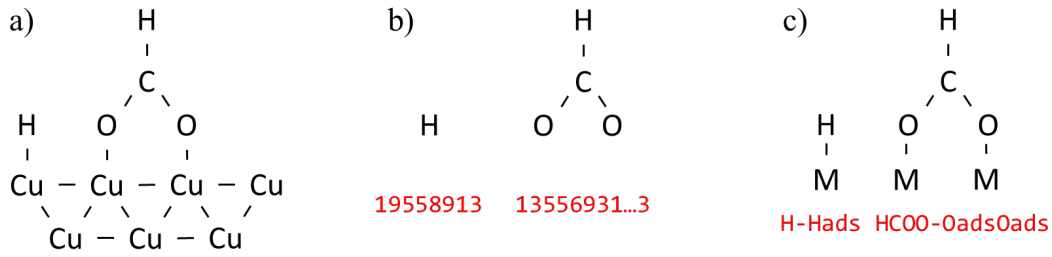

Figure S3. a) the Bond matrix of a H+HCOO on Cu surface, b) bond matrix utilized in ECFP-4 generation, c) and bond matrix utilized in chemical name generation.

all duplicate reactions with higher reaction barriers in the database can be safely removed.

1.4 Fast pathway filter

As described in the main text, the fast pathway filter uses "resistance" as weight in Dijkstra or Yen algorithm to search for low energy reaction pathways. In the following, we will derive **Eq. 1 to 4** in the main text. Different from the derivation of the previous work of Chen et al.[7], we provide a simpler way to derive the resistance.

Consider a simple two-step sequential reaction as an example.

$$\mathrm{A(g)} + 2* \rightleftharpoons 2\mathrm{B}* \tag{S1}$$

$$\mathrm{B}* \rightleftharpoons \mathrm{C(g)} + * \tag{S2}$$

The absolute reaction rate r_1 and r_2 for the reaction 1 and 2 can be written as

$$\boldsymbol{r_1 = \frac{k_b T}{h} exp\left(-\frac{G_{a_1}^{+}}{k_b T}\right)\theta_*^2 - \frac{k_b T}{h} exp\left(-\frac{G_{a_1}^{-}}{k_b T}\right)\theta_{B*}^2} \tag{S3}$$

$$\boldsymbol{r_2 = \frac{k_b T}{h} exp\left(-\frac{G_{a_2}^{+}}{k_b T}\right)\theta_{B*} - \frac{k_b T}{h} exp\left(-\frac{G_{a_2}^{-}}{k_b T}\right)\theta_*} \tag{S4}$$

where $\boldsymbol{G_{a_1}^{+}}$ and $\boldsymbol{G_{a_2}^{+}}$ is the forward Gibbs free energy barrier, and $\boldsymbol{G_{a_1}^{-}}$ and $\boldsymbol{G_{a_2}^{-}}$ is the backward Gibbs free energy barrier. The pressure of A and C gas molecule is implicitly taken into account in Gibbs free energy barriers. Obviously, the barrier terms can further be written as:

$$\boldsymbol{G_{a_1}^{+} = G_1^{\neq} - G_A - 2G_*} \tag{S5}$$

$$\boldsymbol{G_{a_1}^{-} = G_2^{\neq} - 2G_{B*}} \tag{S6}$$

$$\boldsymbol{G_{a_2}^{+} = G_2^{\neq} - G_{B*}} \tag{S7}$$

$$\boldsymbol{G_{a_2}^{-} = G_2^{\neq} - G_C - G_*} \tag{S8}$$

$\boldsymbol{G_1^{\neq}}$ and $\boldsymbol{G_2^{\neq}}$ is Gibbs free energy of the transition state for reaction 1 and 2, respectively, and $\boldsymbol{G_A}$, $\boldsymbol{G_{B*}}$, $\boldsymbol{G_C}$ and $\boldsymbol{G_*}$ is Gibss free energy of corresponding species. $\boldsymbol{G_*}$ can be set as zero.

Thus **Eq. S3** can be written as:

$$\boldsymbol{r_1 = \frac{k_b T}{h} exp\left(-\frac{G_1^{\neq} - G_A - 2G_*}{k_b T}\right)\theta_*^2 - \frac{k_b T}{h} exp\left(-\frac{G_1^{\neq} - 2G_{B*}}{k_b T}\right)\theta_{B*}^2} \tag{S9}$$

Defining "current" as $\mathbf{I_i} = \boldsymbol{r_i}\left(\frac{k_bT}{h}\right)^{-1}$:

$$\boldsymbol{I_1 = exp\left(-\frac{G_1^{\neq} - G_A - 2G_*}{k_bT}\right)\theta_*^2 - exp\left(-\frac{G_1^{\neq} - 2G_{B*}}{k_bT}\right)\theta_{B*}^2} \quad (\boldsymbol{S10})$$

We can further use the "chemical potential" of species $\boldsymbol{i}$, $\boldsymbol{\mu_i}$, to simplify the above formula, where the chemical potential is defined as the Gibbs free energy corrected by the coverage for species, if required. With the following definitions:

$$\boldsymbol{\mu_i = G_i + k_bTln(\theta_i),\ \ for\ i\ is\ adsorbate\ or\ free\ site} \quad (\boldsymbol{S11})$$

$$\boldsymbol{\mu_i = G_i,\ \ for\ i\ is\ gas\ molecule} \quad (\boldsymbol{S12})$$

$$\boldsymbol{\mu_i^{\neq} = G_i,\ \ for\ i\ is\ transition\ state} \quad (\boldsymbol{S13})$$

Eq. S10 can be simplified to:

$$\boldsymbol{I_1 = exp\left(-\frac{\mu_1^{\neq} - \mu_A - 2\mu_*}{k_bT}\right) - exp\left(-\frac{\mu_1^{\neq} - 2\mu_{B*}}{k_bT}\right)} \quad (\boldsymbol{S14})$$

Let's extract the common factors of $\boldsymbol{exp\left(-\frac{\mu_1^{\neq}}{k_bT}\right)}$, I_1 can then be written as

$$\boldsymbol{I_1 = \frac{exp\left(\frac{\mu_A + 2\mu_*}{k_bT}\right) - exp\left(\frac{2\mu_{B*}}{k_bT}\right)}{exp\left(\frac{\mu_1^{\neq}}{k_bT}\right)}} \quad (\boldsymbol{S15})$$

Similarly, **Eq. S4** can also be rewritten to:

$$\boldsymbol{I_2 = \frac{exp\left(\frac{\mu_{B*}}{k_bT}\right) - exp\left(\frac{\mu_C + \mu_*}{k_bT}\right)}{exp\left(\frac{\mu_2^{\neq}}{k_bT}\right)}} \quad (\boldsymbol{S16})$$

The numerator and denominator are multiplied by the same value of $\boldsymbol{exp\left(\frac{\mu_{B*}}{k_bT}\right)}$ or $\boldsymbol{exp\left(\frac{\mu_C+\mu_*}{k_bT}\right)}$, which leads to:

$$\begin{aligned}\boldsymbol{I_2} &= \boldsymbol{\frac{exp\left(\frac{2\mu_{B*}}{k_bT}\right) - exp\left(\frac{\mu_{B*} + \mu_C + \mu_*}{k_bT}\right)}{exp\left(\frac{\mu_2^{\neq} + \mu_{B*}}{k_bT}\right)}} \\ &= \boldsymbol{\frac{exp\left(\frac{\mu_{B*} + \mu_C + \mu_*}{k_bT}\right) - exp\left(\frac{2(\mu_C + \mu_*)}{k_bT}\right)}{exp\left(\frac{\mu_2^{\neq} + \mu_C + \mu_*}{k_bT}\right)}}\end{aligned} \quad (\boldsymbol{S17})$$

Combining the three fractions in **Eq. S15** and **Eq. S17**, we can obtain:

$$\boldsymbol{I_{tot} = 2I_1 = I_2 = \frac{exp\left(\frac{\mu_A + 2\mu_*}{k_bT}\right) - exp\left(\frac{2\mu_C + 2\mu_*}{k_bT}\right)}{exp\left(\frac{\mu_1^{\neq}}{k_bT}\right)/2 + exp\left(\frac{\mu_2^{\neq} + \mu_{B*}}{k_bT}\right) + exp\left(\frac{\mu_2^{\neq} + \mu_C + \mu_*}{k_bT}\right)}} \quad (\boldsymbol{S18})$$

Note that $\boldsymbol{exp\left(\frac{\mu_1^{\neq}}{k_bT}\right)}$ is divided by two, the stoichiometric ratio, to maintain $\mathbf{2I_1 = I_2}$.

Eq.S18 can be interpreted using the reaction profile. As shown by the Gibbs free energy profile in **Figure S4**, we can find the one-to-one correspondence between **Figure S4** and **Eq. S18**. While it is a two-step reaction, there are actually three steps in the energy profile. For the three terms in the denominator of **Eq. S18**, each corresponds to a transition state peak in **Figure S4** (e.g., $\boldsymbol{exp\left(\frac{\mu_2^{\neq}+\mu_{B*}}{k_bT}\right)}$ and $TS_2^{\neq} + B*$). For the two terms in the numerator **Eq. S18**, they correspond to the reactant ($A + 2*$) and product($2C + 2*$) in **Figure S4**. In fact, the two intermediates in the energy profile ($2B*$ and $B* + C +*$) also correspond to the similar terms in **Eq. S15** and **Eq. S17** ($\boldsymbol{exp\left(\frac{2\mu_{B*}}{k_bT}\right)}$ and $\boldsymbol{exp\left(\frac{\mu_{B*}+\mu_C+\mu_*}{k_bT}\right)}$), but they are eventually eliminated in **Eq. S18**.

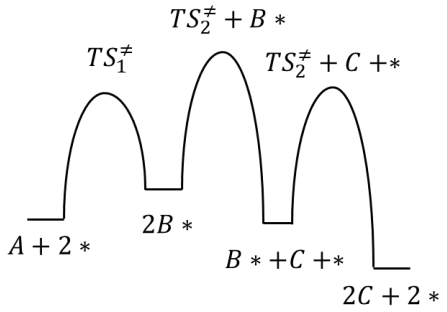

Figure S4. Gibbs free energy profile of the reactions in Eq. S1 and S2.

In **Eq. S18** we can further move $\boldsymbol{exp\left(\frac{2\mu_*}{k_bT}\right)}$ from numerator to denominator to make the numerator independent of the steady state coverage:

$$\boldsymbol{I_{tot} = \frac{exp\left(\frac{\mu_A}{k_bT}\right) - exp\left(\frac{2\mu_C}{k_bT}\right)}{exp\left(\frac{\mu_1^{\neq} - 2\mu_*}{k_bT}\right)/2 + exp\left(\frac{\mu_2^{\neq} + \mu_{B*} - 2\mu_*}{k_bT}\right) + exp\left(\frac{\mu_2^{\neq} + \mu_C - \mu_*}{k_bT}\right)}} \quad (\boldsymbol{S19})$$

Eq. S19 follows Ohm's Law:

$$\boldsymbol{I_{tot} = \frac{U_{reac} - U_{prod}}{R_{tot}}} \quad (\boldsymbol{S20})$$

It means that, with the fixed chemical potential of μ_A and μ_C (only controlled by pressure and temperature and they are all fixed in our microkinetics), the reaction rate or current is then controlled by the total resistance R_{tot}: the higher the resistance is, the lower the current and the reaction rate are.

$$\boldsymbol{R_{tot} = exp\left(\frac{\mu_1^{\neq} - 2\mu_*}{k_bT}\right)/2 + exp\left(\frac{\mu_2^{\neq} + \mu_{B*} - 2\mu_*}{k_bT}\right) + exp\left(\frac{\mu_2^{\neq} + \mu_C - \mu_*}{k_bT}\right)} \quad (\boldsymbol{S21})$$

R_{tot} can be written as the sum of $\boldsymbol{R_i}$ for each reaction $\boldsymbol{i}$,

$$R_{tot} = \sum_i R_i \tag{S22}$$

where the formula of R_i can be generalized as:

$$\boldsymbol{R_i = exp\left(\frac{\mu_i^{\neq} + \sum_j^{spec} \mu_j - n_* \mu_*}{k_b T}\right)} \tag{S23}$$

Thus the resistance of reaction i is controlled by the sum of transition state chemical potential ($\mu_i^{\neq}$) and the chemical potential of spectators ($\sum_j^{spec} \mu_j$), subtracted by the chemical potential of the free site (μ_*) multiplying the number of it involved in the step (n_*). The $\boldsymbol{\mu_j}$ is controlled by barrier height as well as species coverages, as shown in **Eq. S11-13**. The stoichiometric term ("divide by two" in **Eq. S21**) can be neglected for its small contribution (equivalent to $k_b T ln N \approx 0.7 k_b T$ when $N = 2$, N it the stoichiometric ratio). **Eq. 1-3** in the main text are thus derived.

In practice, microkinetics simulation is needed to solve **Eq. S23** to achieve the steady state, where different elementary reaction couples with each other via the coverage term. However, if the coverage contribution to chemical potential can be neglected by setting them to one, **Eq. S23** decays to:

$$\boldsymbol{R_i' = exp\left(\frac{G_i^{\neq} + \sum_j^{spec} G_j}{k_b T}\right)} \tag{S24}$$

which can be used as the weight in Yen and Dijkstra algorithms for fast pathway filter. An advantage of using Eq. S24 is that R_i' is now independent of other reactions, which fulfills the requirement of Dijkstra algorithm that the weight must be independent of trajectory.

It is more convenient to use resistance instead of reaction rate for ranking reaction pathways since the rate can be zero for different products and thus does not distinguish the intermediate in different pathways: the rate is only meaningful when the reaction database is complete.

2 Free Energy corrections

2.1 Gibbs free energy computation

To construct Gibbs free energy profiles based on DFT energetics (e.g. Figure 4), the following procedure is utilized to correct the thermodynamics. For the gas molecules, the vibrational zero-point energy (ZPE), the enthalpy change from 0 K to the finite temperature, and the entropy are considered by using the standard thermodynamics data, if possible, or from DFT calculations. The contribution of pressure is considered with the ideal gas approximation. For surface states, only ZPE of intermediate has been considered. For solid or clean surfaces, the DFT energy is taken as Gibbs free energy directly, since the enthalpy change to finite temperatures, and the entropy for surfaces are negligibly small. All vibrational ZPEs are calculated by using the finite-displacement method using DFT with the displacement step being 0.015 Å. Experimental formation energies, enthalpy changes, and entropies for CO, CO_2, H_2, and H_2O are taken from NIST-JANAF Thermochemical Tables[8]. Experimental formation energies for ZnO and CH_3OH are taken from the NIST Chemistry handbook[9]. Enthalpy change and entropy of CH_3OH are calculated from DFT[10].

In MMLPS, the Gibbs free energies for different pathways are utilized for comparison, where the entropy contribution for non-adsorbed gas molecules including H_2, H_2O, CO_2, CO, and CH_3OH is added to G-NN energetics and the other terms are neglected.

2.2 Additional corrections for molecule DFT energetics

It is well known[11] that Gibbs free energy changes for CO2 and CO hydrogenation to methanol from common DFT calculations, including PBE, BEEF-vdW, and HSE06, generally differ from the experiment data as high as a few tenths of eV. This will inevitably lead to the wrong rate as inferred from **SI, Section 1.**4, especially **Eq. S19** and **Eq. S20** and the additional correction to molecule DFT energetics is the common approach.

As listed in **Table S1** and **Table S2**, in this work, leaving PBE energies of CO_2, H_2, and H_2O unchanged, we take additional energy corrections of -0.44 eV and -0.08 eV for gas-phase CO and CH_3OH, respectively, to maintain the experimental reaction enthalpy change for CO_2 and CO hydrogenation at the standard state. Similar corrections can be found in literatures[12–15] which use BEEF-vdW functional.

It should be mentioned that the above correction can fix the too-strong adsorption of CO on the Cu surface. It is known that CO's adsorption energy (<-0.90) on Cu(111) is overestimated by PBE, concerning the experimental value of -0.49 eV[16], which will lead to nearly full coverage of CO* and inhibit the reaction at 500K. With the -0.44 eV correction, the CO's adsorption energy is closer to the experimental value and avoids CO*'s poisoning on the Cu surface in microkinetics.

Table S1. Energy and correction for gas molecules.

	CO	CO_2	H_2	H_2O	CH_3OH
$\Delta H^{\circ\,\mathrm{exp}}_f(298K)$	-1.14	-4.08	0.00	-2.51	-2.12
PBE-D3 energy	-14.78	-22.96	-6.77	-14.22	-30.20
BEEF-vdW energy	-15.37	-23.30	-7.46	-14.70	-31.63
ZPE	0.13	0.31	0.27	0.57	1.36
$H°(298K) - U(0K)$	0.09	0.10	0.09	0.10	0.09
PBE-D3 Correction	-0.44	-	-	-	-0.05
BEEF-vdW Correction	-	0.33	0.09	-	-

Table S2. Reaction enthalpy for CO_2 and CO hydrogenation with and without correction.

	CO_2 Hydrogenation		CO Hydrogenation	
Energy / eV	ΔH(298K)	error	ΔH(298K)	error
Experiment	-0.55		-0.98	
PBE-D3	-0.50	0.05	-1.36	-0.38
PBE-D3 Correted	-0.55	0.00	-0.97	0.01
BEEF-vdW	0.00	0.55	-0.82	0.16
BEEF-vdW Corrected	-0.60	-0.05	-1.00	-0.02

3 Equations for constructing thermodynamics phase diagram

Under reaction conditions CuZn surface alloy is formed by the reaction of:

$$\mathrm{Cu_n}(surf) + xZnO(s) + xCO(g) - -Cu_{n-x}Zn_x(surf) + xCO_2(g) + xCu(s) \quad (S25)$$

The reaction Gibbs free energy change, $\Delta G_{Cu_{n-x}Zn_x}(T,p)$ or simplified as $\Delta G_{CuZn}(T,P)$, can be evaluated by:

$$\Delta G_{CuZn}(T,P) = G^{surf}_{Cu_{n-x}Zn_x}(T,p) - G^{surf}_{Cu_n}(T,p) + xG^{bulk}_{Cu}(T,p) - xG^{bulk}_{ZnO}(T,p) + x\left[G_{CO_2}(T,p) - G_{CO}(T,p)\right] \quad (S26)$$

This formula can also be written as:

$$\Delta G_{CuZn}(T,P) = G^{surf}_{Cu_{n-x}Zn_x}(T,p) - G^{surf}_{Cu_n}(T,p) + xG^{bulk}_{Cu}(T,p) - xG^{bulk}_{ZnO}(T,p) + x\left[G^{bulk}_{ZnO}(T,p) - G^{bulk}_{Zn}(T,p)\right] + x\left[G_{CO_2}(T,p) - G_{CO}(T,p) + G^{bulk}_{Zn}(T,p) - G^{bulk}_{ZnO}(T,p)\right] \quad (S27)$$

We note the last square bracket is the gain of O chemical potential, $\Delta\mu_O(T,p)$,

$$\Delta\mu_O(T,p) = G_{CO_2}(T,p) + G^{bulk}_{Zn}(T,p) - G_{CO}(T,p) - G^{bulk}_{ZnO}(T,p) \quad (S28)$$

which has the experimental data for the reaction of CO(g)+ZnO(s)= CO2(g)+Zn(s):

$$\Delta\mu_O(T,p) = \Delta\mu^{exp}_O(T,p) = G^{exp}_{CO_2}(T,p) - G^{exp}_{CO}(T,p) + H^{bulk,exp}_{Zn}(298\mathrm{K}) - H^{bulk,exp}_{ZnO}(298K) \quad (S29)$$

where $G^{exp}_{CO_2}(\mathrm{T,p})$ and $G^{exp}_{CO}(T,p)$ are experimental Gibbs free energy of CO2 and CO made by the Shomate equation, whose parameters are obtained by NIST Chemistry Book[9]. $H^{bulk,exp}_{ZnO}(298\mathrm{K})$ and $H^{bulk,exp}_{Zn}(298\mathrm{K})$ are experimental formation enthalpy of ZnO and Zn[17]. Contribution of entropy and enthalpy change for ZnO and Zn bulk is neglected.

Using **Eq. S29**, the last two brackets in **Eq. S27** can be written as the chemical potential of the O atom:

$$\mu_O(T,p) = G^{bulk,DFT}_{ZnO}(T,p) - G^{bulk,DFT}_{Zn}(T,p) + \Delta\mu^{exp}_O(T,p) \quad (S30)$$

and thus **Eq. S27** can be written as:

$$\Delta G_{CuZn}(T,P) = G^{surf,DFT}_{Cu_{n-x}Zn_x}(T,p) - G^{surf,DFT}_{Cu_n}(T,p) + x\left[G^{bulk,DFT}_{Cu}(T,p) - G^{bulk,DFT}_{ZnO}(T,p) + \mu_O(T,p)\right] \quad (S31)$$

Further taking into account the surface area, we divide $\Delta G_{CuZn}(T,P)$ by the number of exposed atoms on the surface layer, n_{layer}:

$$\Delta\gamma_{CuZn}(T,P) = \frac{\Delta G_{CuZn}(T,P)}{n_{layer}} \quad (S32)$$

where n_{layer} is always 9 for the supercells Cu(111), Cu(211), and their surface alloys utilized in this work.

This formula is used to judge the stability of the ZnCu surface alloy model in **Figure 2** in the main text, where Cu(111) and Cu(211) are utilized as the reference for their CuZn alloy surfaces. The phase with minimal $\Delta\gamma_{CuZn}(T,P)$ is the thermodynamically favored phase**.** Note that in **Eq. S30**, $\Delta\mu^{exp}_O(T,p)$ is derived from experimental data.

Similarly, when hydrogen is involved in a phase, e.g., $Zn_6O_7H_7$/Cu(111) model in **Figure 6**, **Eq. S32** can be extended to

$$\Delta G_{\mathrm{Zn_xO_yH_z/Cu(111)}}(T,P) = G^{surf,DFT}_{\mathrm{Zn_xO_yH_z/Cu(111)}}(T,p) - G^{surf,DFT}_{Cu(111)}(T,p) - x\left[G^{bulk,DFT}_{ZnO}(T,p) - \mu_O(T,p)\right] - y\mu_O(T,p) - \frac{z}{2}G^{DFT}_{H_2}(T,p) \quad (S33)$$

Considering the surface area:

$$\Delta\gamma_{\mathrm{Zn_xO_yH_z/Cu(111)}}(T,P) = \frac{\Delta G_{\mathrm{Zn_xO_yH_z/Cu(111)}}(T,P)}{n_{layer}} \quad (S34)$$

where n_{layer} is 36 (p(6x6)) for $\mathrm{Zn_6O_7H_7/Cu(111)}$ model utilized in this work. The phase with the minimal

$\Delta\gamma_{CuZn}(T,P)$ or $\Delta\gamma_{Zn_xO_yH_z/Cu(111)}(T,P)$ at a given temperature and pressure among Cu(111), Cu(211), their surface alloy, and $Zn_6O_7H_7$/Cu(111) is plotted in **Figure 6c**.

4 SSW-NN method and global neural network (G-NN) potential

4.1 NN potential architecture

The G-NN potential utilized in this work follows the atom-centered high dimensional neural network (HDNN) architecture[18], whose input layer is constructed by power type structural descriptor (PTSD) as discussed in our previous works[19–21]. The total energy E^{tot} of the structure can be composed as a linear combination of its atomic energy E_i from the output of NN

$$E^{tot} = \sum_i E_i \tag{S35}$$

Consistently, the atomic force can be analytically derived from the total energy, i.e., the force component $F_{k,\alpha}$ (α = x, y, or z) acting on atom k is the derivative of the total energy E^{tot} with respect to the coordinate $\mathrm{R}_{k,\alpha}$. In combination with **Eq. S35**, the force component $F_{k,\alpha}$ then is related to the derivatives of the atomic energy E_i with respect to the jth structural descriptors of atom i, $G_{j,i}$

$$F_{k,\alpha} = -\frac{\partial E^{tot}}{\partial \mathrm{R}_{k,\alpha}} = -\sum_{i,j} \frac{\partial E_i}{\partial G_{j,i}} \frac{\partial G_{j,i}}{\partial \mathrm{R}_{k,\alpha}} \tag{S36}$$

Similarly, the element $\sigma_{\alpha\beta}$ of static stress tensor matrix can be analytically derived as

$$\sigma_{\alpha\beta} = -\frac{1}{V} \sum_{i,j,d} \frac{(\boldsymbol{r}_d)_\alpha (\boldsymbol{r}_d)_\beta}{r_d} \frac{\partial E_i}{\partial G_{j,i}} \frac{\partial G_{j,i}}{\partial r_d} \tag{S37}$$

where $\boldsymbol{r}_d$ and r_d is the distance vector, constituted by $G_{j,i}$ and its module, respectively, and V is the volume of the structure.

The limited-memory Broyden-Fletcher-Goldfarb-Shannon (L-BFGS) method is used to minimize the loss function to match DFT energy, force, and stress.

4.2 SSW-NN method

SSW-NN method is a machine-learning potential based global optimization method, which combines the global neural network (G-NN) potential with SSW method for fast and accurate global PES exploration as implemented in LASP code.[22] While traditional DFT calculations are frustrating for the global optimization of complex systems due to the high computational cost, SSW-NN method provides a general solution for PES scanning with both high efficiency and high accuracy.[23] The G-NN potential is trained based on SSW dataset calculated using DFT and delivers a high speed of PES evaluation, 3~4 orders of magnitude faster than DFT.[19–21]

4.3 Dataset generation and self-learning NN training

We utilized the stochastic surface walking (SSW) global optimization to generate a global dataset, which is fully automated and does not need a priori knowledge of the system, such as the structural motif, e.g. bonding patterns and symmetry. The final obtained Cu-Zn-C-H-O global dataset contains a variety of structural patterns on the global PES, as summarized in **Table S3**. In brief, the SSW-NN method involves three stages to generate the global dataset, as described below.

(i) **The first stage** generates a raw dataset, which contains the most common atomic environment and serves to build an initial NN PES. This is done by performing density functional theory (DFT) SSW global optimization in a massively parallel way. In this stage, the DFT calculations have low accuracy setups and small unit cells to speed up the SSW search. By collecting and screening the structures from SSW trajectories, a raw dataset is obtained.

(ii) **The second stage** trains a NN global PES. This is done by refining the dataset using DFT calculations with

high accuracy setups, followed by NN training on the accurate global dataset. The NN architecture applied in this stage utilizes a small set of structural descriptors and a small network size.

(iii) **The third stage** iteratively expands the global dataset. It targets to increase the predictive power of NN PES by incorporating more structural patterns into the dataset. This is done by performing SSW PES search using the NN PES obtained in the second stage, starting from a variety of initial structures. These initial structures are randomly constructed, and also include large systems with many atoms per unit cell. The structures from all the SSW trajectories are collected and filtered to generate an additional dataset. The new dataset is then fed to the global dataset to start a new cycle of NN training (back to the second stage).

4.4 Benchmark of G-NN calculations

A benchmark of G-NN calculations with DFT calculations on 2400 structures is plotted in **Figure S5**. The structures are randomly selected from the reaction pair dataset sampled by automated SSW-RS (300 structures including IS, TS & FS per sampling process and each process starts with molecules of CO_2+H_2, HCOOH+H_2 or HCHO+ H_2 and slabs of Cu(111), Cu(211), 0.11 ML Zn-Cu(211), 0.22 ML Zn-Cu(211). The x-axis is the window of energy relative to CO_2+$3H_2$ reactants, while energy for H_2, $2H_2$, or H_2O is added for mass balance. It can be seen that theese structures has a normal distribution centered on the energy of CO_2+$3H_3$ reactant, and the RMSE for energy in between G-NN results and DFT results are all below 2.10 meV/atom for each energy interval. It suggests that the G-NN potential has a good accuracy in identifying the low energy surface reactions.

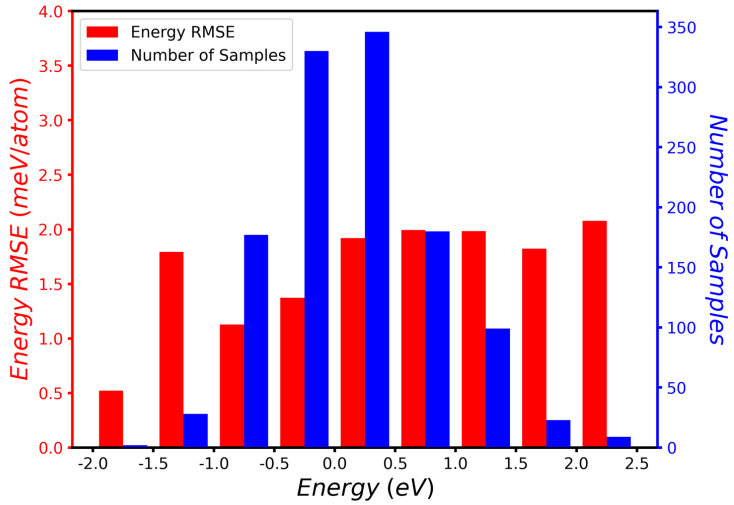

Figure S5. Energy RMSEs between G-NN and DFT for 2400 structures randomly selected from reaction database, including IS, TS and FS. The x-axis energy is relative to that of CO_2+$3H_2$ reactant.

Table S3. Structure information of the global dataset for NN training. Listed data are the number of the structures in the global dataset, as distinguished by the chemical formula, the number of atoms(Natom), the type of structures (cluster, bulk, layer), and the total number (Ntotal).

Species	Natom	cluster	layer	bulk	Ntotal
Zn14	14	0	1	10	11
Zn15	15	18	3	235	256
Zn16	16	361	52	1184	1597
Zn17	17	0	0	3	3
Zn19	19	0	24	0	24

Zn22	22	0	27	0	27
Zn24	24	0	3	112	115
Zn28	28	0	0	10	10
Zn29	29	0	3	0	3
Zn30	30	0	9	12	21
Zn31	31	0	0	28	28
Zn32	32	0	1	28	29
Cu2-Zn13	15	0	0	2	2
Cu2-Zn14	16	0	0	2	2
Cu3-Zn11	14	0	0	1	1
Cu3-Zn12	15	0	0	3	3
Cu3-Zn13	16	1	0	7	8
Cu4-Zn4	8	0	31	9	40
Cu4-Zn11	15	0	0	5	5
Cu4-Zn12	16	14	0	36	50
Cu5-Zn9	14	0	0	3	3
Cu5-Zn10	15	0	0	19	19
Cu5-Zn11	16	15	0	100	115
Cu6-Zn9	15	4	0	46	50
Cu6-Zn10	16	40	2	204	246
Cu6-Zn13	19	0	2	0	2
Cu7-Zn7	14	0	0	4	4
Cu7-Zn8	15	5	0	43	48
Cu7-Zn9	16	48	3	223	274
Cu7-Zn10	17	0	0	2	2
Cu7-Zn15	22	0	1	0	1
Cu7-Zn17	24	0	0	1	1
Cu8-Zn6	14	0	1	2	3
Cu8-Zn7	15	4	1	52	57
Cu8-Zn8	16	50	4	261	315
Cu8-Zn16	24	0	0	1	1
Cu8-Zn40	48	0	37	8	45
Cu9-Zn5	14	0	0	3	3
Cu9-Zn6	15	5	1	40	46
Cu9-Zn7	16	50	5	240	295
Cu9-Zn10	19	0	1	0	1
Cu9-Zn15	24	0	0	3	3
Cu9-Zn21	30	0	1	0	1
Cu10-Zn4	14	0	0	1	1
Cu10-Zn5	15	2	1	19	22
Cu10-Zn6	16	54	1	174	229
Cu10-Zn7	17	0	0	1	1
Cu10-Zn9	19	0	3	0	3
Cu10-Zn12	22	0	1	0	1
Cu10-Zn14	24	0	0	7	7
Cu11-Zn4	15	1	0	10	11
Cu11-Zn5	16	16	1	87	104
Cu11-Zn8	19	0	1	0	1
Cu11-Zn13	24	0	0	10	10
Cu11-Zn18	29	0	1	0	1
Cu11-Zn19	30	0	1	2	3
Cu11-Zn20	31	0	0	1	1
Cu11-Zn21	32	0	1	1	2
Cu12-Zn3	15	1	0	3	4

Cu12-Zn4	16	7	0	90	97
Cu12-Zn7	19	0	1	0	1
Cu12-Zn12	24	0	0	5	5
Cu12-Zn17	29	0	1	0	1
Cu12-Zn19	31	0	0	1	1
Cu13-Zn3	16	1	1	67	69
Cu13-Zn9	22	0	1	0	1
Cu13-Zn11	24	0	0	5	5
Cu13-Zn16	29	0	3	0	3
Cu13-Zn18	31	0	0	2	2
Cu13-Zn19	32	0	0	1	1
Cu14	14	0	1	16	17
Cu14-Zn2	16	0	1	57	58
Cu14-Zn3	17	0	0	1	1
Cu14-Zn10	24	0	0	4	4
Cu14-Zn14	28	0	0	2	2
Cu14-Zn15	29	0	2	0	2
Cu14-Zn16	30	0	1	2	3
Cu14-Zn17	31	0	0	3	3
Cu14-Zn18	32	0	0	2	2
Cu15	15	39	3	470	512
Cu15-Zn9	24	0	0	4	4
Cu15-Zn13	28	0	0	1	1
Cu15-Zn14	29	0	3	0	3
Cu15-Zn15	30	0	2	1	3
Cu15-Zn16	31	0	0	2	2
Cu15-Zn17	32	0	0	2	2
Cu16	16	561	41	2823	3425
Cu16-Zn6	22	0	1	0	1
Cu16-Zn8	24	0	0	3	3
Cu16-Zn12	28	0	0	1	1
Cu16-Zn14	30	0	1	3	4
Cu16-Zn15	31	0	0	4	4
Cu16-Zn16	32	0	32	7	39
Cu17	17	0	0	17	17
Cu17-Zn11	28	0	0	2	2
Cu17-Zn13	30	0	3	0	3
Cu17-Zn14	31	0	0	3	3
Cu17-Zn15	32	0	0	6	6
Cu18-Zn10	28	0	0	1	1
Cu18-Zn11	29	0	1	0	1
Cu18-Zn12	30	0	1	0	1
Cu18-Zn13	31	0	0	1	1
Cu18-Zn14	32	0	1	1	2
Cu19-Zn11	30	0	2	0	2
Cu19-Zn13	32	0	0	4	4
Cu20-Zn4	24	0	1	0	1
Cu20-Zn10	30	0	1	0	1
Cu20-Zn11	31	0	0	1	1
Cu20-Zn12	32	0	78	7	85
Cu21-Zn8	29	0	1	0	1
Cu21-Zn10	31	0	0	1	1
Cu21-Zn11	32	0	0	1	1
Cu23-Zn7	30	0	0	1	1

Cu24-Zn8	32	0	31	8	39
Cu28	28	0	0	14	14
Cu29	29	0	9	0	9
Cu30	30	0	25	17	42
Cu31	31	0	0	45	45
Cu32	32	0	0	60	60
O1-Cu5-Zn11	17	0	0	1	1
O1-Cu6-Zn10	17	0	0	1	1
O1-Cu7-Zn9	17	0	0	2	2
O1-Cu8-Zn8	17	0	1	1	2
O1-Cu9-Zn7	17	0	0	1	1
O1-Cu16	17	0	1	19	20
O2-Zn17	19	0	4	82	86
O2-Cu4-Zn12	18	0	0	1	1
O2-Cu5-Zn11	18	0	0	1	1
O2-Cu6-Zn10	18	0	0	2	2
O2-Cu6-Zn11	19	0	0	5	5
O2-Cu7-Zn9	18	0	0	2	2
O2-Cu7-Zn10	19	0	0	4	4
O2-Cu8-Zn8	18	0	0	2	2
O2-Cu8-Zn9	19	0	0	7	7
O2-Cu9-Zn7	18	0	0	2	2
O2-Cu9-Zn8	19	0	0	10	10
O2-Cu10-Zn7	19	0	0	6	6
O2-Cu12-Zn4	18	0	1	0	1
O2-Cu12-Zn5	19	0	0	2	2
O2-Cu13-Zn4	19	0	0	1	1
O2-Cu16	18	0	2	31	33
O2-Cu20-Zn7	29	0	2	0	2
O2-Cu22-Zn5	29	0	3	0	3
O2-Cu24-Zn3	29	0	2	0	2
O3-Cu5-Zn11	19	0	0	1	1
O3-Cu6-Zn10	19	0	0	3	3
O3-Cu7-Zn9	19	0	1	1	2
O3-Cu9-Zn7	19	0	0	2	2
O3-Cu10-Zn6	19	0	0	1	1
O3-Cu11-Zn5	19	0	0	1	1
O3-Cu16	19	0	2	16	18
O4	4	0	47	0	47
O4-Zn15	19	0	0	9	9
O4-Cu2-Zn14	20	0	0	2	2
O4-Cu4-Zn11	19	0	0	1	1
O4-Cu6-Zn10	20	0	2	0	2
O4-Cu8-Zn8	20	0	0	1	1
O4-Cu9-Zn6	19	0	0	1	1
O4-Cu9-Zn7	20	0	0	4	4
O4-Cu10-Zn6	20	0	0	2	2
O4-Cu11-Zn5	20	0	0	1	1
O4-Cu16	20	0	4	20	24
O4-Cu20-Zn8	32	0	35	4	39
O6-Zn4	10	0	0	15	15
O6-Zn6	12	550	0	0	550
O6-Zn8	14	0	7	102	109
O6-Cu1-Zn3	10	0	0	94	94

O6-Cu1-Zn5	12	16	0	0	16
O6-Cu2-Zn2	10	0	0	119	119
O6-Cu2-Zn4	12	30	0	0	30
O6-Cu2-Zn6	14	0	0	3	3
O6-Cu3-Zn1	10	0	0	91	91
O6-Cu3-Zn3	12	48	0	0	48
O6-Cu3-Zn5	14	0	0	4	4
O6-Cu4	10	0	0	1496	1496
O6-Cu4-Zn2	12	30	0	0	30
O6-Cu4-Zn4	14	0	0	4	4
O6-Cu5-Zn1	12	18	0	0	18
O6-Cu5-Zn3	14	0	0	10	10
O6-Cu6	12	2	0	0	2
O6-Cu6-Zn2	14	0	0	1	1
O6-Cu6-Zn10	22	0	0	1	1
O6-Cu7-Zn9	22	0	0	7	7
O6-Cu8-Zn8	22	0	0	4	4
O6-Cu9-Zn7	22	0	0	3	3
O6-Cu10-Zn6	22	0	0	3	3
O6-Cu11-Zn5	22	0	0	3	3
O6-Cu13-Zn3	22	0	0	1	1
O6-Cu16	22	0	1	47	48
O6-Cu45-Zn13	64	0	25	0	25
O7-Zn8	15	0	6	116	122
O7-Zn16	23	0	0	14	14
O7-Cu1-Zn7	15	0	0	9	9
O7-Cu2-Zn6	15	0	0	28	28
O7-Cu3-Zn5	15	0	0	45	45
O7-Cu4-Zn4	15	0	1	53	54
O7-Cu5-Zn3	15	0	0	44	44
O7-Cu6-Zn2	15	0	1	27	28
O7-Cu7-Zn1	15	0	1	10	11
O7-Cu8	15	0	0	619	619
O7-Cu45-Zn13	65	0	27	0	27
O8-Zn8	16	150	54	1869	2073
O8-Cu1-Zn7	16	0	0	20	20
O8-Cu2-Zn6	16	5	0	82	87
O8-Cu3-Zn5	16	13	0	197	210
O8-Cu4-Zn4	16	12	0	253	265
O8-Cu5-Zn3	16	9	0	193	202
O8-Cu5-Zn11	24	0	0	1	1
O8-Cu6-Zn2	16	5	0	96	101
O8-Cu6-Zn10	24	0	1	3	4
O8-Cu7-Zn1	16	1	0	25	26
O8-Cu8	16	0	0	1274	1274
O8-Cu8-Zn8	24	0	0	1	1
O8-Cu9-Zn7	24	0	1	1	2
O8-Cu10-Zn6	24	0	0	2	2
O8-Cu11-Zn5	24	0	0	1	1
O8-Cu12-Zn4	24	0	0	1	1
O8-Cu16	24	0	8	31	39
O8-Cu16-Zn8	32	0	28	9	37
O8-Cu45-Zn13	66	0	16	0	16
O8-Cu47-Zn11	66	0	242	5	247

O10-Zn10	20	0	500	44	544
O10-Zn16	26	0	0	33	33
O10-Zn24	34	0	6	123	129
O10-Cu2-Zn8	20	0	5	1	6
O10-Cu3-Zn7	20	0	18	3	21
O10-Cu4-Zn6	20	0	35	5	40
O10-Cu5-Zn5	20	0	42	3	45
O10-Cu5-Zn11	26	0	0	1	1
O10-Cu6-Zn4	20	0	29	1	30
O10-Cu6-Zn10	26	0	0	50	50
O10-Cu7-Zn3	20	0	11	1	12
O10-Cu8-Zn2	20	0	7	0	7
O10-Cu8-Zn8	26	0	0	2	2
O10-Cu8-Zn16	34	0	0	2	2
O10-Cu9-Zn1	20	0	1	0	1
O10-Cu9-Zn7	26	0	0	2	2
O10-Cu9-Zn15	34	0	1	4	5
O10-Cu10-Zn6	26	0	0	1	1
O10-Cu10-Zn14	34	0	1	5	6
O10-Cu11-Zn5	26	0	0	1	1
O10-Cu11-Zn13	34	0	0	7	7
O10-Cu12-Zn12	34	0	0	13	13
O10-Cu13-Zn11	34	0	0	5	5
O10-Cu14-Zn10	34	0	0	4	4
O10-Cu15-Zn9	34	0	0	3	3
O10-Cu16	26	0	1	16	17
O10-Cu16-Zn8	34	0	1	1	2
O10-Cu17-Zn7	34	0	0	2	2
O10-Cu18-Zn6	34	0	0	1	1
O11	11	0	247	68	315
O11-Zn15	26	0	0	9	9
O11-Zn16	27	0	11	0	11
O11-Cu5-Zn11	27	0	1	0	1
O11-Cu8-Zn7	26	0	0	1	1
O11-Cu8-Zn8	27	0	1	1	2
O11-Cu9-Zn7	27	0	1	0	1
O11-Cu11-Zn5	27	0	0	1	1
O11-Cu16	27	0	0	6	6
O12-Cu5-Zn11	28	0	0	1	1
O12-Cu6-Zn10	28	0	0	2	2
O12-Cu7-Zn9	28	0	0	4	4
O12-Cu8-Zn8	28	0	0	1	1
O12-Cu9-Zn7	28	0	0	2	2
O12-Cu10-Zn6	28	0	0	2	2
O12-Cu16	28	0	1	20	21
O12-Cu24-Zn24	60	0	37	10	47
O13-Zn15	28	0	60	13	73
O13-Cu3-Zn12	28	0	1	0	1
O13-Cu4-Zn11	28	0	1	0	1
O13-Cu4-Zn12	29	0	1	57	58
O13-Cu5-Zn10	28	0	1	0	1
O13-Cu6-Zn9	28	0	3	0	3
O13-Cu7-Zn8	28	0	5	2	7
O13-Cu8-Zn7	28	0	2	2	4

O13-Cu9-Zn6	28	0	6	2	8
O13-Cu12-Zn3	28	0	0	1	1
O13-Cu13-Zn2	28	0	1	0	1
O14-Zn15	29	0	0	26	26
O14-Zn16	30	0	72	20	92
O14-Cu4-Zn12	30	0	1	0	1
O14-Cu5-Zn11	30	0	1	0	1
O14-Cu6-Zn9	29	0	0	2	2
O14-Cu6-Zn10	30	0	3	1	4
O14-Cu7-Zn8	29	0	0	1	1
O14-Cu7-Zn9	30	0	1	0	1
O14-Cu8-Zn7	29	0	0	2	2
O14-Cu8-Zn8	30	0	3	1	4
O14-Cu9-Zn6	29	0	0	1	1
O14-Cu9-Zn7	30	0	3	0	3
O14-Cu10-Zn5	29	0	0	1	1
O14-Cu10-Zn6	30	0	2	1	3
O14-Cu11-Zn5	30	0	2	0	2
O14-Cu12-Zn4	30	0	0	1	1
O14-Cu14-Zn2	30	0	1	0	1
O14-Cu16	30	0	1	16	17
O15-Cu7-Zn9	31	0	0	1	1
O15-Cu8-Zn8	31	0	0	2	2
O15-Cu9-Zn7	31	0	0	2	2
O15-Cu16	31	0	1	26	27
O16-Zn14	30	0	140	5	145
O16-Zn16	32	0	156	61	217
O16-Cu3-Zn13	32	0	1	0	1
O16-Cu4-Zn10	30	0	6	0	6
O16-Cu4-Zn12	32	0	2	1	3
O16-Cu5-Zn9	30	0	3	1	4
O16-Cu5-Zn11	32	0	4	3	7
O16-Cu6-Zn8	30	0	8	0	8
O16-Cu6-Zn10	32	0	2	2	4
O16-Cu7-Zn7	30	0	9	1	10
O16-Cu7-Zn9	32	0	3	7	10
O16-Cu8-Zn6	30	0	6	0	6
O16-Cu8-Zn8	32	0	12	5	17
O16-Cu9-Zn5	30	0	6	0	6
O16-Cu9-Zn7	32	0	13	3	16
O16-Cu10-Zn4	30	0	1	0	1
O16-Cu10-Zn6	32	0	10	54	64
O16-Cu11-Zn3	30	0	2	0	2
O16-Cu11-Zn5	32	0	3	3	6
O16-Cu12-Zn4	32	0	2	0	2
O16-Cu16	32	0	6	15	21
O16-Cu16-Zn16	48	0	24	9	33
O16-Cu64-Zn16	96	0	655	3	658
O17-Cu11-Zn5	33	0	0	41	41
O21-Cu1-Zn24	46	0	2	0	2
O21-Cu13-Zn24	58	0	61	3	64
O22-Cu6-Zn10	38	0	0	3	3
O22-Cu7-Zn9	38	0	0	9	9
O22-Cu8-Zn8	38	0	0	7	7

O22-Cu8-Zn24	54	0	224	0	224
O22-Cu9-Zn7	38	0	0	6	6
O22-Cu10-Zn6	38	0	0	2	2
O22-Cu11-Zn5	38	0	1	63	64
O22-Cu12-Zn4	38	0	0	2	2
O22-Cu16	38	0	0	97	97
O23-Cu1-Zn24	48	0	7	3	10
O23-Cu13-Zn24	60	0	13	53	66
O24-Cu1-Zn24	49	0	1	5	6
O24-Cu3-Zn22	49	0	7	0	7
O24-Cu5-Zn11	40	0	0	1	1
O24-Cu6-Zn26	56	0	127	0	127
O24-Cu8-Zn24	56	0	116	0	116
O24-Cu10-Zn22	56	0	121	0	121
O24-Cu12-Zn22	58	0	34	1	35
O24-Cu16	40	0	0	7	7
O24-Cu16-Zn24	64	0	220	0	220
O26-Cu14-Zn24	64	0	184	0	184
C1-O25-Cu8-Zn24	58	0	26	0	26
C1-O25-Cu16-Zn24	66	0	197	0	197
H1-C1-O6-Cu48-Zn6	62	0	11	0	11
H1-C1-O25-Cu16-Zn24	67	0	58	0	58
H2-O1-Cu27	30	0	144	0	144
H2-O24-Cu10-Zn22	58	0	32	0	32
H2-C1-O2-Cu5-Zn11	21	0	1	0	1
H2-C1-O2-Cu8-Zn8	21	0	2	0	2
H2-C1-O2-Cu9-Zn7	21	0	4	0	4
H2-C1-O2-Cu10-Zn6	21	0	8	0	8
H2-C1-O2-Cu11	16	0	1	6	7
H2-C1-O2-Cu11-Zn5	21	0	12	0	12
H2-C1-O2-Cu12	17	0	4630	250	4880
H2-C1-O2-Cu12-Zn4	21	0	12	0	12
H2-C1-O2-Cu13-Zn3	21	0	25	0	25
H2-C1-O2-Cu14-Zn2	21	0	22	0	22
H2-C1-O2-Cu15-Zn1	21	0	19	0	19
H2-C1-O2-Cu15-Zn12	32	0	1	0	1
H2-C1-O2-Cu16	21	0	182	0	182
H2-C1-O2-Cu16-Zn11	32	0	1	0	1
H2-C1-O2-Cu17-Zn10	32	0	2	0	2
H2-C1-O2-Cu18-Zn9	32	0	4	0	4
H2-C1-O2-Cu19-Zn8	32	0	2	0	2
H2-C1-O2-Cu20-Zn7	32	0	21	0	21
H2-C1-O2-Cu21-Zn6	32	0	7	0	7
H2-C1-O2-Cu22-Zn5	32	0	7	0	7
H2-C1-O2-Cu23-Zn4	32	0	19	0	19
H2-C1-O2-Cu24-Zn3	32	0	205	0	205
H2-C1-O2-Cu25-Zn2	32	0	263	0	263
H2-C1-O2-Cu26-Zn1	32	0	5	0	5
H2-C1-O2-Cu27	32	0	191	0	191
H2-C1-O5-Cu41-Zn13	62	0	71	0	71
H2-C1-O5-Cu43-Zn11	62	0	67	0	67
H2-C1-O5-Cu45-Zn9	62	0	34	0	34
H2-C1-O5-Cu46-Zn8	62	0	14	0	14
H2-C1-O5-Cu48-Zn6	62	0	18	0	18

H2-C1-O6-Cu45-Zn9	63	0	59	0	59
H2-C1-O23-Cu8-Zn24	58	0	70	0	70
H2-C1-O25-Cu6-Zn26	60	0	30	0	30
H2-C2-O3-Cu13-Zn14	34	0	1	0	1
H2-C2-O3-Cu14-Zn13	34	0	1	0	1
H2-C2-O3-Cu15-Zn12	34	0	3	0	3
H2-C2-O3-Cu16-Zn11	34	0	4	0	4
H2-C2-O3-Cu17-Zn10	34	0	29	0	29
H2-C2-O3-Cu18-Zn9	34	0	25	0	25
H2-C2-O3-Cu19-Zn8	34	0	17	0	17
H2-C2-O3-Cu20-Zn7	34	0	33	0	33
H2-C2-O3-Cu21-Zn6	34	0	25	0	25
H2-C2-O3-Cu22-Zn5	34	0	21	0	21
H2-C2-O3-Cu23-Zn4	34	0	57	0	57
H2-C2-O3-Cu24-Zn3	34	0	34	0	34
H2-C2-O3-Cu25-Zn2	34	0	24	0	24
H2-C2-O3-Cu26-Zn1	34	0	17	0	17
H2-C2-O3-Cu27	34	0	409	0	409
H2-C2-O3-Cu36	43	0	601	0	601
H2-C3-O4-Cu33	42	0	228	0	228
H2-C3-O4-Cu35	44	0	215	0	215
H2-C3-O4-Cu36	45	0	457	0	457
H3-C1-O2-Cu9-Zn9	24	0	1	0	1
H3-C1-O2-Cu10-Zn8	24	0	3	0	3
H3-C1-O2-Cu11-Zn7	24	0	5	0	5
H3-C1-O2-Cu12-Zn6	24	0	5	0	5
H3-C1-O2-Cu13-Zn5	24	0	16	0	16
H3-C1-O2-Cu14-Zn4	24	0	5	0	5
H3-C1-O2-Cu15-Zn3	24	0	8	0	8
H3-C1-O2-Cu16-Zn2	24	0	15	0	15
H3-C1-O2-Cu17-Zn1	24	0	14	0	14
H3-C1-O2-Cu18	24	0	148	0	148
H3-C1-O5-Cu40-Zn14	63	0	80	0	80
H3-C1-O5-Cu41-Zn13	63	0	613	4	617
H3-C1-O5-Cu43-Zn11	63	0	1739	1	1740
H3-C1-O5-Cu45-Zn9	63	0	79	0	79
H3-C1-O6-Cu45-Zn9	64	0	92	0	92
H3-C1-O7-Cu42-Zn10	63	0	43	1	44
H3-C1-O8-Cu40-Zn11	63	0	40	1	41
H3-C1-O25-Cu11-Zn29	69	0	155	0	155
H3-C1-O25-Cu13-Zn27	69	0	107	0	107
H3-C1-O25-Cu16-Zn24	69	0	511	0	511
H3-C1-O25-Cu19-Zn21	69	0	122	0	122
H3-C2-O2-Cu31	38	0	3	0	3
H3-C2-O2-Cu32	39	0	2	0	2
H3-C2-O2-Cu36	43	0	254	0	254
H3-C2-O3-Cu13-Zn14	35	0	3	1	4
H3-C2-O3-Cu14-Zn10	32	0	2	0	2
H3-C2-O3-Cu15-Zn8	31	0	1	0	1
H3-C2-O3-Cu15-Zn9	32	0	1	0	1
H3-C2-O3-Cu17-Zn7	32	0	2	0	2
H3-C2-O3-Cu18-Zn5	31	0	3	0	3
H3-C2-O3-Cu18-Zn6	32	0	4	0	4
H3-C2-O3-Cu18-Zn9	35	0	1	0	1

H3-C2-O3-Cu19-Zn4	31	0	1	0	1
H3-C2-O3-Cu19-Zn5	32	0	7	0	7
H3-C2-O3-Cu20-Zn3	31	0	1	0	1
H3-C2-O3-Cu20-Zn4	32	0	1	0	1
H3-C2-O3-Cu21-Zn3	32	0	1	0	1
H3-C2-O3-Cu21-Zn6	35	0	5	0	5
H3-C2-O3-Cu22-Zn1	31	0	4	0	4
H3-C2-O3-Cu22-Zn2	32	0	14	0	14
H3-C2-O3-Cu22-Zn5	35	0	1	0	1
H3-C2-O3-Cu23	31	0	15	0	15
H3-C2-O3-Cu24	32	0	60	3	63
H3-C2-O3-Cu26-Zn1	35	0	2	0	2
H3-C2-O3-Cu27	35	0	23	0	23
H3-C2-O6-Cu42-Zn12	65	0	42	0	42
H3-C2-O6-Cu43-Zn11	65	0	239	0	239
H4-O24-Cu16-Zn24	68	0	201	0	201
H4-C1-O1-Cu12	18	0	301	0	301
H4-C1-O3-Cu11-Zn16	35	0	1	0	1
H4-C1-O3-Cu12-Zn15	35	0	1	0	1
H4-C1-O3-Cu13-Zn14	35	0	5	0	5
H4-C1-O3-Cu14-Zn13	35	0	7	0	7
H4-C1-O3-Cu15-Zn12	35	0	21	0	21
H4-C1-O3-Cu16-Zn11	35	0	18	0	18
H4-C1-O3-Cu17-Zn10	35	0	45	0	45
H4-C1-O3-Cu18-Zn9	35	0	97	1	98
H4-C1-O3-Cu19-Zn8	35	0	142	2	144
H4-C1-O3-Cu20-Zn7	35	0	97	0	97
H4-C1-O3-Cu21-Zn6	35	0	74	1	75
H4-C1-O3-Cu22-Zn5	35	0	126	1	127
H4-C1-O3-Cu23-Zn4	35	0	105	0	105
H4-C1-O3-Cu24-Zn3	35	0	170	1	171
H4-C1-O3-Cu25-Zn2	35	0	124	0	124
H4-C1-O3-Cu26-Zn1	35	0	63	0	63
H4-C1-O3-Cu27	35	0	1698	0	1698
H4-C1-O5-Cu41-Zn13	64	0	607	2	609
H4-C1-O5-Cu42-Zn12	64	0	202	0	202
H4-C1-O5-Cu43-Zn11	64	0	369	1	370
H4-C1-O5-Cu44-Zn10	64	0	393	2	395
H4-C1-O5-Cu45-Zn9	64	0	33	1	34
H4-C1-O5-Cu46-Zn8	64	0	8	0	8
H4-C1-O6-Cu42-Zn11	64	0	646	7	653
H4-C1-O6-Cu43-Zn11	65	0	106	1	107
H4-C1-O7-Cu38-Zn14	64	0	36	0	36
H4-C1-O7-Cu42-Zn10	64	0	37	0	37
H4-C2-O2-Cu18-Zn9	35	0	1	0	1
H4-C2-O2-Cu21-Zn6	35	0	4	0	4
H4-C2-O2-Cu22-Zn5	35	0	2	0	2
H4-C2-O2-Cu27	35	0	21	0	21
H4-C2-O2-Cu33	41	0	183	0	183
H4-C2-O2-Cu36	44	0	174	0	174
H4-C2-O3-Cu36	45	0	79	0	79
H4-C2-O4-Cu2-Zn10	22	0	4	1	5
H4-C2-O4-Cu4-Zn8	22	0	0	1	1
H4-C2-O4-Cu5-Zn7	22	0	2	4	6

H4-C2-O4-Cu6-Zn6	22	0	3	16	19
H4-C2-O4-Cu7-Zn4	21	0	1	0	1
H4-C2-O4-Cu7-Zn5	22	0	48	58	106
H4-C2-O4-Cu8-Zn3	21	0	2	1	3
H4-C2-O4-Cu8-Zn4	22	0	76	101	177
H4-C2-O4-Cu9-Zn3	22	0	113	165	278
H4-C2-O4-Cu10-Zn2	22	0	133	210	343
H4-C2-O4-Cu11	21	0	4	5	9
H4-C2-O4-Cu11-Zn1	22	0	104	265	369
H4-C2-O4-Cu12	22	0	70	1798	1868
H4-C2-O4-Cu13-Zn14	37	0	1	0	1
H4-C2-O4-Cu15-Zn9	34	0	1	0	1
H4-C2-O4-Cu15-Zn12	37	0	8	0	8
H4-C2-O4-Cu16-Zn8	34	0	3	0	3
H4-C2-O4-Cu16-Zn11	37	0	4	0	4
H4-C2-O4-Cu17-Zn10	37	0	37	1	38
H4-C2-O4-Cu18-Zn6	34	0	7	0	7
H4-C2-O4-Cu18-Zn9	37	0	79	3	82
H4-C2-O4-Cu19-Zn5	34	0	4	0	4
H4-C2-O4-Cu19-Zn7	36	0	3	0	3
H4-C2-O4-Cu19-Zn8	37	0	42	1	43
H4-C2-O4-Cu20-Zn4	34	0	6	1	7
H4-C2-O4-Cu20-Zn7	37	0	42	1	43
H4-C2-O4-Cu21-Zn3	34	0	8	1	9
H4-C2-O4-Cu21-Zn6	37	0	101	4	105
H4-C2-O4-Cu22-Zn2	34	0	11	0	11
H4-C2-O4-Cu22-Zn5	37	0	82	6	88
H4-C2-O4-Cu23-Zn1	34	0	5	0	5
H4-C2-O4-Cu23-Zn4	37	0	53	1	54
H4-C2-O4-Cu24	34	0	87	11	98
H4-C2-O4-Cu24-Zn2	36	0	1	0	1
H4-C2-O4-Cu24-Zn3	37	0	55	3	58
H4-C2-O4-Cu25-Zn1	36	0	3	0	3
H4-C2-O4-Cu25-Zn2	37	0	65	1	66
H4-C2-O4-Cu26	36	0	13	0	13
H4-C2-O4-Cu26-Zn1	37	0	41	0	41
H4-C2-O4-Cu27	37	0	780	0	780
H4-C2-O4-Cu32	42	0	29	0	29
H4-C2-O4-Cu36	46	0	545	0	545
H4-C2-O6-Cu43-Zn11	66	0	37	0	37
H4-C2-O25-Cu16-Zn24	71	0	509	0	509
H4-C3-O5-Cu36	48	0	11	0	11
H5-C1-O2-Cu15-Zn8	31	0	1	0	1
H5-C1-O2-Cu19-Zn4	31	0	4	0	4
H5-C1-O2-Cu23	31	0	2	0	2
H5-C1-O6-Cu44-Zn8	64	0	278	0	278
H6-C1-O1-Cu13-Zn14	35	0	3	0	3
H6-C1-O1-Cu16-Zn11	35	0	12	0	12
H6-C1-O1-Cu17-Zn10	35	0	3	0	3
H6-C1-O1-Cu18-Zn9	35	0	6	0	6
H6-C1-O1-Cu19-Zn8	35	0	9	0	9
H6-C1-O1-Cu20-Zn7	35	0	10	0	10
H6-C1-O1-Cu21-Zn6	35	0	12	0	12
H6-C1-O1-Cu22-Zn5	35	0	6	0	6

H6-C1-O1-Cu23-Zn4	35	0	12	0	12
H6-C1-O1-Cu24-Zn3	35	0	657	0	657
H6-C1-O1-Cu25-Zn2	35	0	1072	0	1072
H6-C1-O1-Cu26-Zn1	35	0	996	0	996
H6-C1-O1-Cu27	35	0	1050	0	1050
H6-C1-O2-Cu14-Zn13	36	0	3	0	3
H6-C1-O2-Cu15-Zn12	36	0	4	0	4
H6-C1-O2-Cu16-Zn11	36	0	44	0	44
H6-C1-O2-Cu17-Zn10	36	0	34	0	34
H6-C1-O2-Cu18-Zn9	36	0	34	0	34
H6-C1-O2-Cu19-Zn8	36	0	49	0	49
H6-C1-O2-Cu20-Zn7	36	0	43	0	43
H6-C1-O2-Cu21-Zn6	36	0	82	1	83
H6-C1-O2-Cu22-Zn5	36	0	63	0	63
H6-C1-O2-Cu23-Zn4	36	0	58	0	58
H6-C1-O2-Cu24-Zn3	36	0	54	1	55
H6-C1-O2-Cu25-Zn2	36	0	134	0	134
H6-C1-O2-Cu26-Zn1	36	0	39	0	39
H6-C1-O2-Cu27	36	0	987	0	987
H6-C1-O3-Cu3-Zn9	22	0	6	1	7
H6-C1-O3-Cu5-Zn7	22	0	1	2	3
H6-C1-O3-Cu6-Zn6	22	0	6	3	9
H6-C1-O3-Cu7-Zn5	22	0	22	69	91
H6-C1-O3-Cu8-Zn4	22	0	21	25	46
H6-C1-O3-Cu9-Zn3	22	0	51	59	110
H6-C1-O3-Cu10-Zn2	22	0	28	78	106
H6-C1-O3-Cu11-Zn1	22	0	56	65	121
H6-C1-O3-Cu12	22	0	33	716	749
H6-C1-O6-Cu40-Zn11	64	0	38	0	38
H6-C1-O6-Cu44-Zn8	65	0	44	0	44
H6-C1-O16-Cu59-Zn18	100	0	189	52	241
H6-C1-O16-Cu62-Zn18	103	0	182	78	260
H6-C2-O3-Cu36	47	0	780	0	780
H6-C2-O16-Cu60-Zn18	102	0	128	112	240
H6-C2-O16-Cu62-Zn18	104	0	122	129	251
H7-O16-Cu58-Zn20	101	0	181	2	183
H7-O16-Cu59-Zn21	103	0	213	0	213
H7-O16-Cu60-Zn20	103	0	198	52	250
H7-O16-Cu61-Zn19	103	0	179	4	183
H7-O16-Cu62-Zn18	103	0	214	50	264
H7-O16-Cu64-Zn16	103	0	685	16	701
H7-O16-Cu67-Zn13	103	0	321	32	353
H8-C1-O2-Cu22-Zn5	38	0	1	0	1
H8-C1-O2-Cu23-Zn4	38	0	1	0	1
H8-C1-O2-Cu26-Zn1	38	0	3	0	3
H8-C1-O2-Cu27	38	0	4	0	4
H8-C2-O2-Cu13-Zn10	35	0	3	0	3
H8-C2-O2-Cu14-Zn10	36	0	3	0	3
H8-C2-O2-Cu16-Zn7	35	0	1	0	1
H8-C2-O2-Cu16-Zn8	36	0	1	0	1
H8-C2-O2-Cu18-Zn5	35	0	5	0	5
H8-C2-O2-Cu19-Zn5	36	0	4	1	5
H8-C2-O2-Cu20-Zn3	35	0	0	1	1
H8-C2-O2-Cu22-Zn2	36	0	2	2	4

H8-C2-O2-Cu23	35	0	6	2	8
H8-C2-O2-Cu24	36	0	20	8	28
H12-C2-O4-Cu4-Zn8	30	0	0	2	2
H12-C2-O4-Cu5-Zn7	30	0	8	6	14
H12-C2-O4-Cu6-Zn6	30	0	18	22	40
H12-C2-O4-Cu7-Zn5	30	0	54	63	117
H12-C2-O4-Cu8-Zn4	30	0	76	106	182
H12-C2-O4-Cu9-Zn3	30	0	90	198	288
H12-C2-O4-Cu10-Zn2	30	0	131	193	324
H12-C2-O4-Cu11-Zn1	30	0	120	239	359
H12-C2-O4-Cu12	30	0	31	2074	2105
H14-O7	21	0	0	253	253
H16-O8	24	0	6	1209	1215
H30-O15	45	41	0	36	77
total	--	2227	36968	24344	63539

5 Global minima structures for 0.44 ML Zn-Cu(211) and Zn-Cu(211)

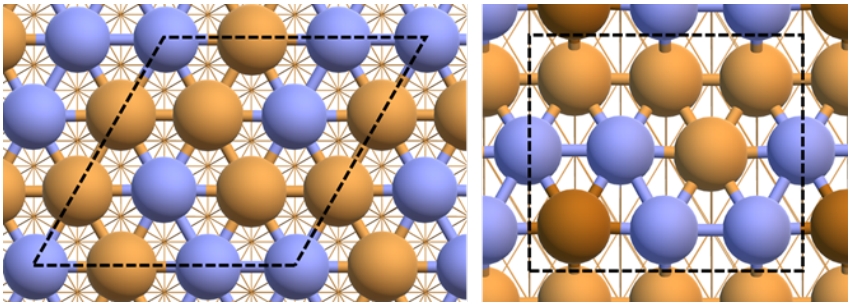

Figure S6. SSW global-optimized structures for 0.44 ML Zn-Cu(211) and 0.44 ML Zn-Cu(211)

6 Reaction pair database: the CVs for viewing and the other information

Collective variables (CVs)[24,25] utilized in **Figure 3** to distinguish different intermediates are described in the following. A coordination function between elements is first defined as

$$c[\mathrm{X}-\mathrm{Y}]=\sum_{ij}\frac{\left[1-\left(\frac{d_{X_iY_j}}{d_{XY}^0}\right)^p\right]}{\left[1-\left(\frac{d_{X_iY_j}}{d_{XY}^0}\right)^{p+q}\right]} \quad (S38)$$

where X and Y represent two elements, $d_{X_iY_j}$ is the distance between atom X_i and Y_j, d_{XY}^0 is cutoff parameters set as 1.10 Å, 1.00 Å, and 0.90 Å for $c[\mathrm{C}-\mathrm{O}]$, $c[\mathrm{C}-\mathrm{H}]$, and $c[\mathrm{O}-\mathrm{H}]$, respectively, and p=16 and q=6 are exponents.

We then use a combination of $c[\mathrm{C}-\mathrm{O}]$, $c[\mathrm{C}-\mathrm{H}]$, and $c[\mathrm{O}-\mathrm{H}]$ as CVs for plotting Figure 3:

$$CV_1=c[C-H]+c[\mathrm{O}-\mathrm{H}] \quad (S39)$$

$$CV_2=c[\mathrm{C}-\mathrm{O}]+0.8c[\mathrm{O}-\mathrm{H}] \quad (S40)$$

Note that all intermediates in dataset are aligned to the same CO_2H_6 formula (by adding virtual H_2 or H_2O for mass balance) as described in **SI, Section 1.2**. For example, CVs of the dataset with COH_4 formula (starting with $HCHO+H_2$) need to add CVs of a gas phase H_2O molecule in plotting **Figure 3**.

Table S4. Statistics for Reaction pair database obtained from MMLPS on all surface studied. "s" notes for spectator whose bond is kept unchanged in MMLPS. n_{cycle}, cycle number of SSW-RS. $n_{min\ cycle}$, the number of minimum for each cycle. $n_{tot\ min}$ the total number of minima. $n_{tot\ pair}$, the total number of reaction pairs. $n_{unq\ species}$ and $n_{unq\ pair}$, the number of unique species and the number of unique reactions after removing the redundancy, respectively.

surface	starting reactants	n_{cycles}	$n_{min\ cycle}$	$n_{tot\ min}$	$n_{tot\ pair}$	$n_{unq\ speci}$	$n_{unq\ pair}$
Cu(111)	CO_2+H_2	14	20000	280000	3193	20	183
	HCOOH+H_2	20	20000	400000	4090	44	570
	HCHO+H_2	14	20000	280000	8456	36	363
Cu(211)	CO_2+H_2	15	20000	300000	2791	23	183
	HCOOH+H_2	31	20000	620000	6258	57	570
	HCHO+H_2	15	20000	300000	5909	35	363
1/9MLZn(Cu211)	CO_2+H_2	15	20000	300000	2716	22	177
	HCOOH+H_2	31	20000	620000	6394	54	543
	HCHO+H_2	15	20000	300000	5264	33	345
2/9MLZn(Cu211)	CO_2+H_2	15	20000	300000	2267	21	153
	HCOOH+H_2	32	20000	640000	5723	58	576
	HCHO+H_2	15	20000	300000	5238	36	378
Cu(211)	HCOO+CO_2+H_2	67	10000	670000	5954	170	1548
	HCOO+HCOOH+H_2	63	10000	630000	3812	243	1491
	HCOO+HCHO+H_2	51	10000	510000	3658	195	1158
1/9MLZn(Cu211)	HCOO+CO_2+H_2	75	10000	750000	6167	172	1620
	HCOO+HCOOH+H_2	40	10000	400000	2305	203	1179
	HCOO+HCHO+H_2	61	10000	610000	4130	217	1281
2/9MLZn(Cu211)	HCOO+CO_2+H_2	78	10000	780000	6772	202	1575
	HCOO+HCOOH+H_2	76	10000	760000	4863	283	1890
	HCOO+HCHO+H_2	78	10000	780000	5361	233	1677
Cu(211)	HCOO(s)+CO_2+H_2	11	10000	110000	1108	47	285
	HCOO(s)+HCOOH+H_2	28	10000	280000	2636	156	957
	HCOO(s)+HCHO+H_2	30	10000	300000	3810	143	990
1/9MLZn(Cu211)	HCOO(s)+CO_2+H_2	12	10000	120000	932	55	285
	HCOO(s)+HCOOH+H_2	30	10000	330000	2402	146	846
	HCOO(s)+HCHO+H_2	33	10000	330000	4755	150	1023
2/9MLZn(Cu211)	HCOO(s)+CO2+H2	3	10000	30000	394	25	99
	HCOO(s)+HCOOH+H_2	27	10000	270000	2426	118	771
	HCOO(s)+HCHO+H2	19	10000	190000	1648	94	525

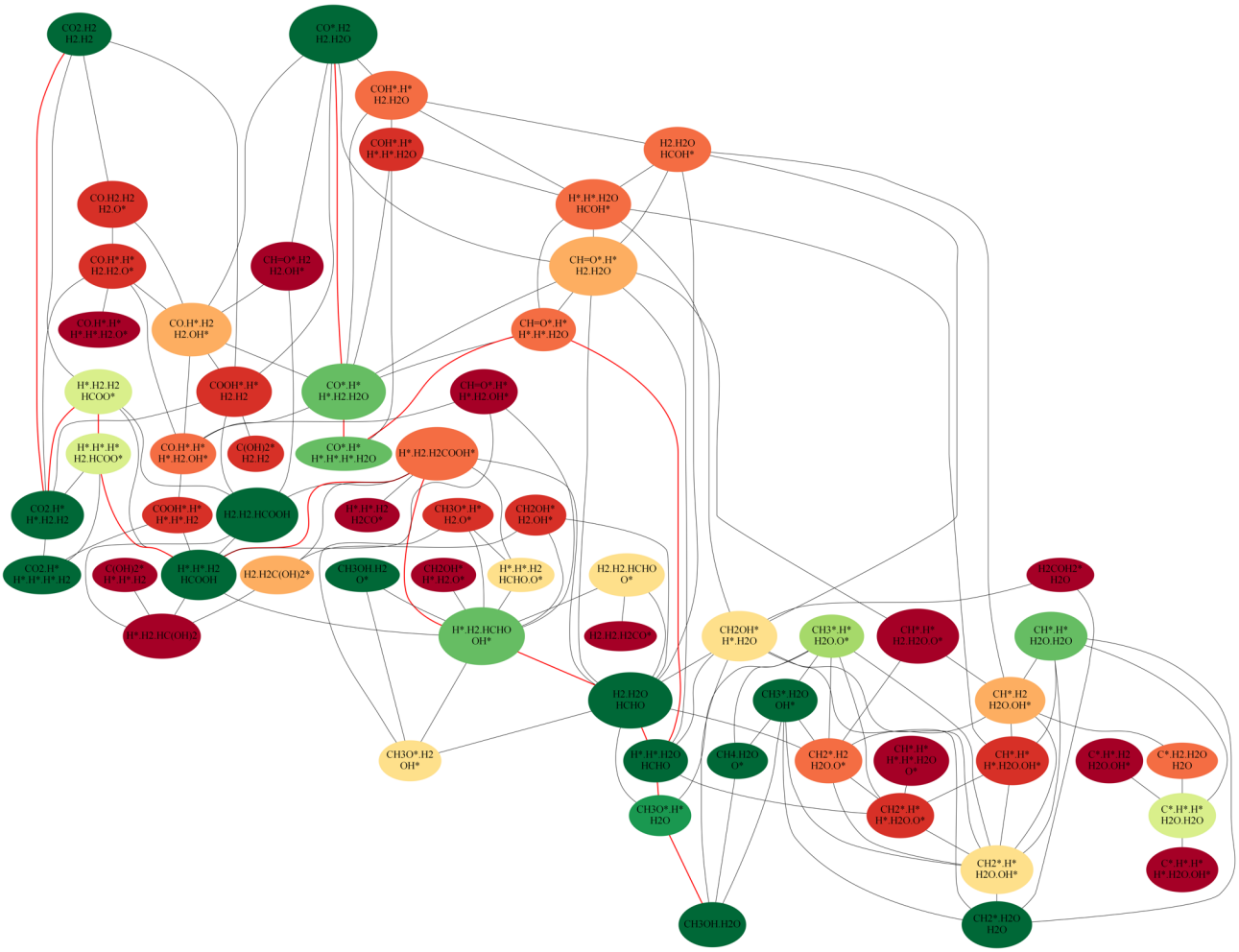

Figure S7. Merged reaction network sampled for CO_2 and CO hydrogenation reaction on Cu(111). In the graph nodes represent intermediates, whose color from green to red implies the Gibbs free energies of intermediate from low to high; edges between nodes represent the reactions between them. The identified lowest energy pathways for CO_2 hydrogenation and CO hydrogenation are marked by red lines.

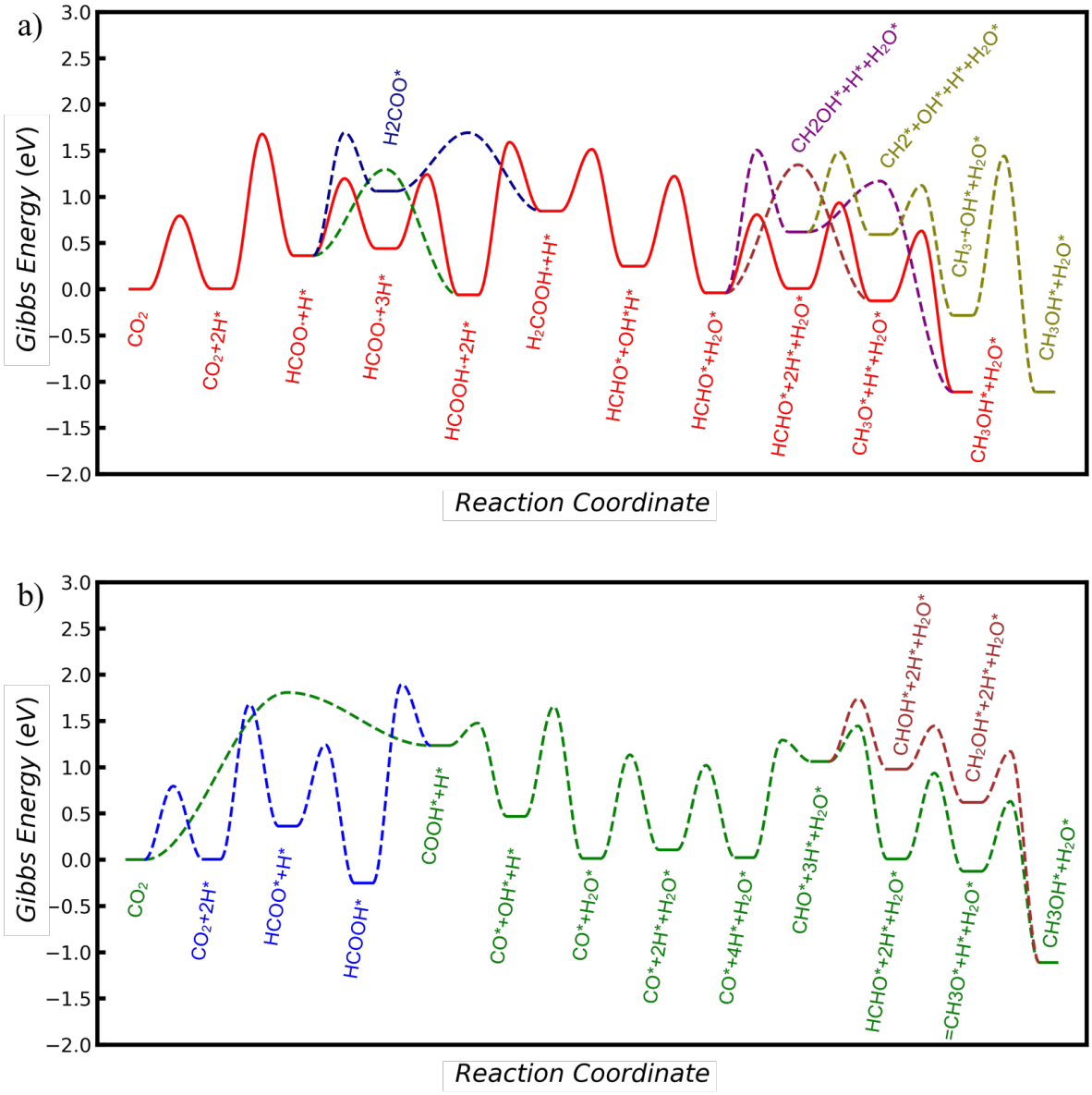

Figure S8. Gibbs energy profile of several minority reaction pathways (dotted lines) for CO_2 hydrogenation on Cu(211) at 500K, 40, 10, 10, 1, 1 bar of H_2, CO_2, CO, CH_3OH and H_2O. The solid line in (a) is the lowest energy pathway shown for comparison. The Gibbs free energy is in G-NN level and corrected with gas molecules' entropies.

7 Gibbs free energy of key species based on DFT energetics

Table S5. DFT total energy and Gibbs free energy (data in parenthesis) of key species (including TS) in CO_2 and CO hydrogenation. The Gibbs free energy is relative to the corresponding clean surface, and the gas molecule CO_2, H_2, and H_2O except those indicated by superscript (a) is relative to CO and H_2. All energies are in eV.

Species / transition state	Cu(111)	Cu(211)	0.11 ML Zn -Cu(211)	0.22 ML Zn -Cu(211)	0.11 ML HCOO*/ Cu(211)	0.11 ML HCOO*/ 0.11 ML Zn-Cu(211)	0.11 ML HCOO*/ 0.22 ML Zn-Cu(211)
H*	-0.35(-0.09)	-0.36(-0.10)	-0.34(-0.09)	-0.27(-0.01)	-0.30(-0.04)	-0.26(+0.00)	-0.17(+0.10)
HCOO*	-0.82(+0.51)	-1.22(+0.12)	-1.26(+0.08)	-1.30(+0.05)	-0.90(+0.45)	-0.91(+0.43)	-0.85(+0.49)
HCOOH*	-0.73(+0.97)	-1.00(+0.71)	-0.91(+0.79)	-0.94(+0.77)	-0.84(+0.89)	-0.82(+0.91)	-0.76(+0.96)
H_2COOH*	-0.90(+1.21)	-1.28(+0.84)	-1.27(+0.85)	-1.33(+0.79)	-1.33(+0.83)	-1.30(+0.85)	-0.97(+1.17)
HCHO*	-0.16(+1.24)	-0.56(+0.83)	-0.53(+0.87)	-0.53(+0.85)	-0.62(+0.81)	-0.59(+0.84)	-0.47(+0.97)
CH_3O*	-1.44(+0.40)	-1.68(+0.15)	-1.74(+0.10)	-1.83(+0.02)	-1.65(+0.20)	-1.66(+0.19)	-1.43(+0.42)
CH_3OH*	-1.62(+0.60)	-1.93(+0.30)	-1.84(+0.37)	-1.67(+0.57)	-1.98(+0.26)	-2.25(+0.01)	-1.65(+0.58)
CO* [a]	-0.67(+0.23)	-0.71(+0.19)	-0.72(+0.18)	-0.68(+0.22)	-0.67(+0.24)	-0.76(+0.59)	-0.57(+0.34)
CHO* [a]	-0.09(+1.16)	-0.27(+0.98)	-0.25(+0.99)	-0.22(+1.02)	-0.21(+1.06)	-0.22(+1.05)	-0.18(+1.09)
$H_2 \rightarrow H^* + H^*$	+0.21(+0.64)	+0.33(+0.76)	+0.34(+0.77)	+0.38(+0.81)	+0.21(+0.64)	+0.35(+0.78)	+0.34(+0.76)
$CO_2 + H^* \rightarrow HCOO^*$	+0.34(+1.48)	+0.17(+1.31)	+0.21(+1.35)	+0.26(+1.40)	+0.13(+1.26)	+0.16(+1.31)	+0.22(+1.37)
$HCOO^* + H^* \rightarrow HCOOH^*$	-0.18(+1.31)	-0.37(+1.11)	-0.42(+1.06)	-0.29(+1.20)	-0.24(+1.27)	-0.17(+1.36)	-0.23(+1.27)
$HCOOH^* + H^* \rightarrow H_2COOH^*$	-0.07(+1.85)	-0.62(+1.29)	-0.62(+1.30)	-0.48(+1.43)	-0.47(+1.48)	-0.43(+1.49)	-0.36(+1.57)
$H_2COOH^* \rightarrow HCHO^* + OH^*$	-0.19(+1.78)	-0.74(+1.28)	-0.78(+1.25)	-0.74(+1.30)	-0.63(+1.43)	-0.68(+1.39)	-0.54(+1.55)
$HCHO^* + H^* \rightarrow CH_3O^*$	-0.30(+1.31)	-0.68(+0.95)	-0.58(+1.07)	-0.57(+1.04)	-0.59(+1.03)	-0.65(+0.98)	-0.60(+1.03)
$CH3O^* + H^* \rightarrow CH_3OH^*$	-0.51(+1.48)	-1.28(+0.72)	-1.25(+0.75)	-1.22(+0.79)	-1.08(+0.93)	-0.91(+1.10)	-0.71(+1.29)
$CO^* + H^* \rightarrow CHO^*$ [a]	+0.02(+1.12)	-0.10(+0.99)	-0.10(+1.02)	-0.05(+1.07)	+0.19(+1.31)	+0.16(+1.33)	+0.20(+1.29)
$CHO^* + H^* \rightarrow HCHO^*$ [a]	+0.11(+1.58)	-0.15(+1.35)	-0.07(+1.42)	-0.01(+1.49)	+0.02(+1.49)	+0.04(+1.51)	+0.05(+1.58)

8 Comparison of reaction barriers with previous studies

Table S6. Comparison of reaction barriers with previous studies*

	Grabow et al.[26] Cu(111) PW91		Kattel et al.[27] 0.11 ML Zn-Cu(211) PW91		Wang et al.[28] 0.11 ML Zn-Cu(211) optPBE-vdW		Wang et al.[28] 0.11 ML Zn-Cu(211) optPBE-vdW		Sun et al.[29] 0.11 ML Zn-Cu(211) PBE-D3	
Reaction	Ea	diff	Ea^{ZPE}	$diff^{ZPE}$	Ea	diff	Ea	diff	Ea^{Gibbs}	$diff^{Gibbs}$
CO_2+H*→HCOO*	0.87	-0.11	0.77	0.08	0.75	0.06	0.59	0.04	1.28	-0.01
HCOO*+H*→HCOOH*	0.91	-0.08	1.19	0.01	1.04	0.05	1.25	0.07	1.07	-0.06
HCOOH*+H*→H_2COOH*	1.04	-0.03	0.61	-0.14	0.85	-0.16	0.69	0.05	0.55	-0.04
H_2COOH*→HCHO*+OH*	0.74	0.03	0.52	0.15	0.77	0.06	0.51	0.02	0.41	-0.17
CO*+H*→CHO*	0.99	-0.08	0.73	-0.19	1.05	0.01	0.97	0.01	0.90	0.00
CHO*+H*→HCHO*	0.47	-0.08	0.69	0.17	0.52	-0.03	0.56	0.04	0.60	0.12
HCHO*+H*→CH3O*	0.24	-0.07	0.12	-0.13	0.34	0.13	0.26	-0.03	0.15	-0.03
CH_3O*+H*→CH_3OH*	1.17	-0.05	1.49	0.73	1.25	-0.03	0.85	0.02	0.71	0.14

Table S7. Comparison of reaction barriers with previous studies*

	Behrens et al.[12] Cu(111) RPBE,		Behrens et al.[12] Cu(211) RPBE,		Behrens et al.[12] 0.11 ML Zn-Cu(211) RPBE,		Wu et al.[15,30] Cu(211) BEEF-vdW		Studt et al[13] Cu(211) RPBE		Studt et al[13] Cu(211) BEEF-vdW	
Reaction	Ea^{ZPE}	$diff^{ZPE}$	Ea^{ZPE}	$diff^{ZPE}$	Ea^{ZPE}	$diff^{ZPE}$	Ea	diff	Ea	diff	Ea	diff
CO_2+H*→HCOO*	0.50	-0.14	0.36	-0.11	0.37	-0.13	0.20	-0.32	0.45	-0.28	0.32	-0.20
HCOO*+H*→HCOOH**	0.84	-0.05	1.32	0.23	1.37	0.31	1.27	0.06	1.31	0.04	1.39	0.19
HCOOH*+H*→H_2COOH*	0.55	-0.43	0.38	-0.30	0.42	-0.17	0.76	0.03	0.14	-0.75	0.49	-0.24
H_2COOH*→HCHO*+OH*	0.63	0.06	0.37	-0.07	0.50	0.10	0.42	-0.12	0.46	-0.08	0.26	-0.27
CO*+H*→CHO* [a]	0.88	-0.10	0.88	-0.02	0.88	-0.04	0.93	-0.04	0.92	-0.12	0.96	-0.01
CHO*+H*→HCHO* [a]	0.45	-0.06	0.57	0.10	0.85	0.33	0.63	0.16	0.57	0.12	0.59	0.11
HCHO*+H*→CH_3O*	0.73	0.56	0.51	0.29	0.47	0.19	0.11	-0.12	0.33	0.01	0.34	0.10
CH_3O*+H*→CH_3OH*	0.94	-0.24	1.27	0.60	1.13	0.39	0.89	0.13	0.81	0.02	0.81	0.06

* All energies are in eV. "E_a" is the forward reaction barrier. The "ZPE" / "Gibbs" superscript indicates that the energy contains the ZPE / Gibbs free energy corrections. "diff" denotes the difference between the barrier from us and from previous works ($E_a^{previous}$- E_a^{our}) at the denoted correction level.

9 Reaction Snapshots for key reaction steps on (Zn-)Cu(211)

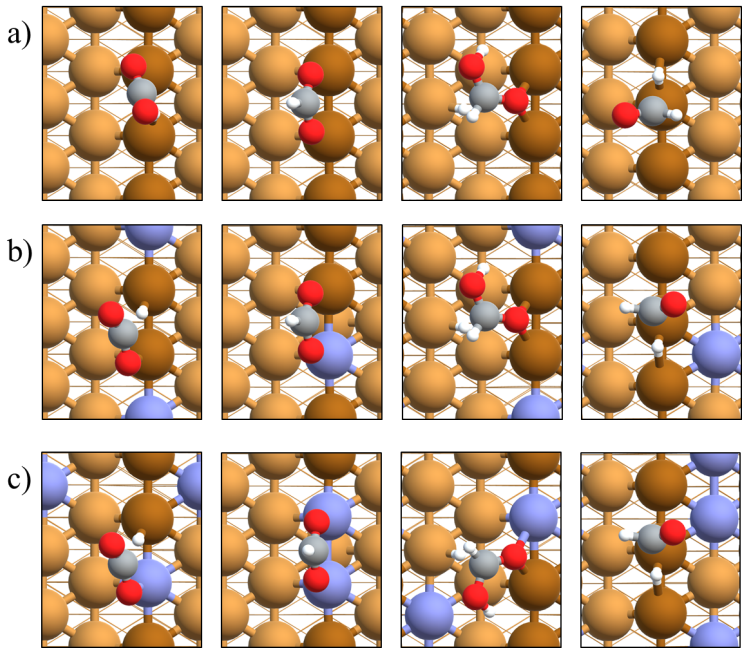

Figure S9. Reaction snapshots for key reaction step including (from left to right) CO2-H*, HCOO*, HCOOH-H*, CHO-H* on surfaces including (from top to bottom) a) Cu(211), b) 0.11 ML Zn-Cu(211), and c) 0.22 ML Zn-Cu(211)

10 Reaction profiles on Cu and CuZn surfaces with HCOO* spectator

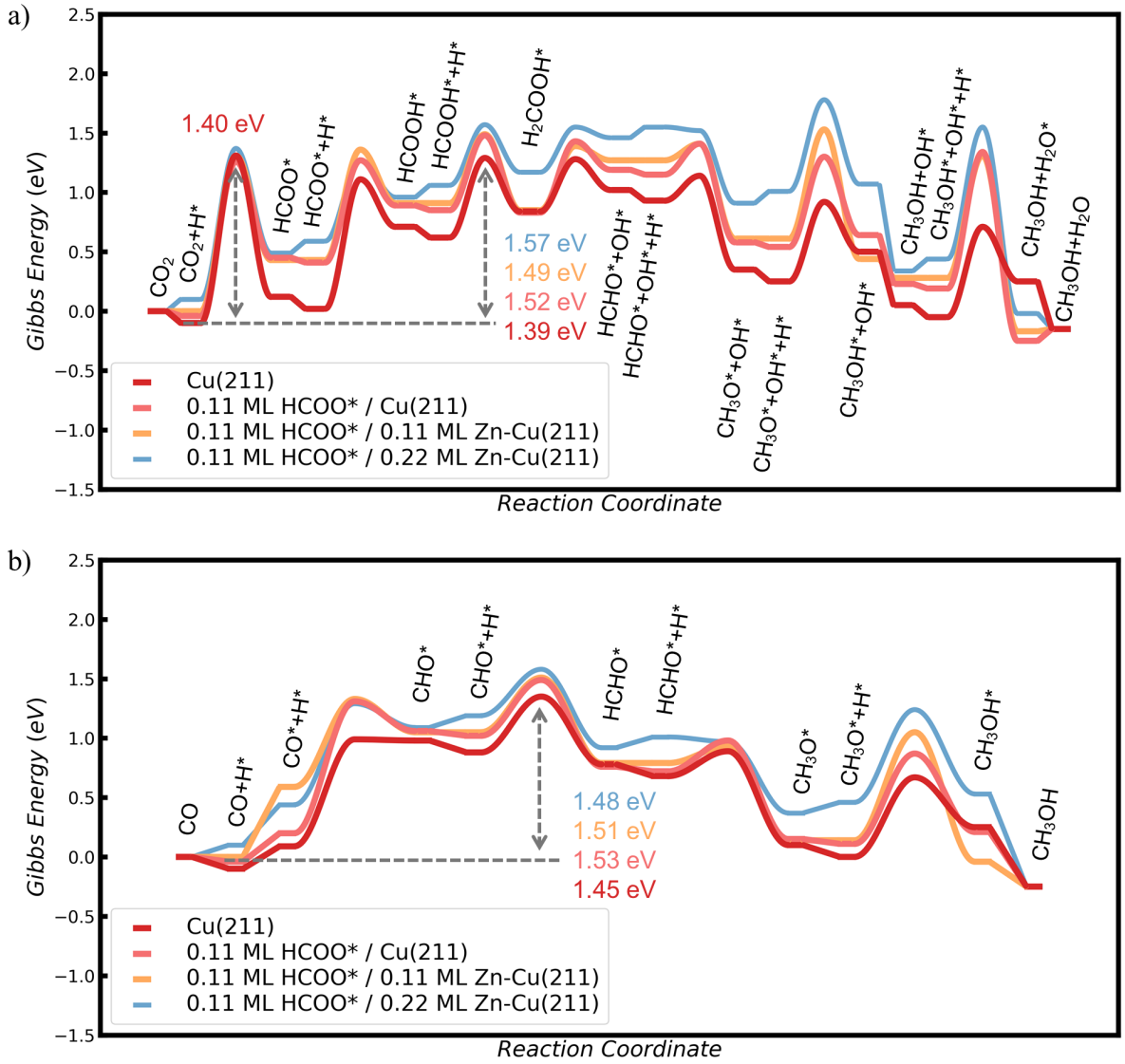

Figure S10. Gibbs energy profiles for a) CO_2 hydrogenation an b) CO hydrogenation on Cu(211) (red), 0.11 ML HCOO* / Cu(211) (light red), 0.11 ML HCOO* / 0.11 ML Zn-Cu(211) (light orange), 0.11 ML HCOO* / 0.22 ML Zn-Cu(211) (light blue) at 500K, 40, 10, 10, 1, 1 bar of H_2, CO_2, CO, CH_3OH and H_2O.

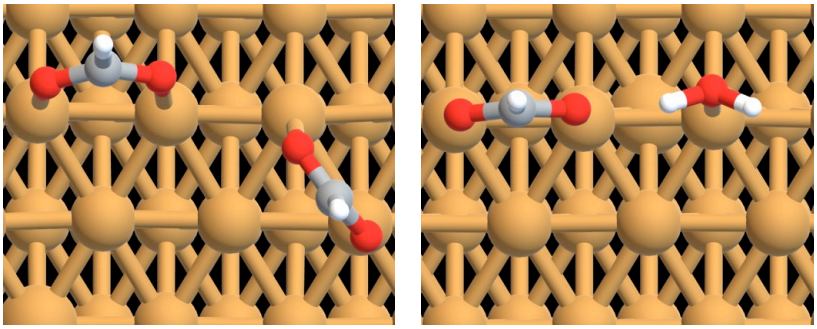

Figure S11. Structure for HCOO* and H_2O* on 0.11 ML HCOO* / Cu(211)

11 Microkinetics simulation results

Table S8. Surface coverage of species in microkinetics simulation on Cu(211) at 500K, 40, 10, 10, 1, 1 bar of H_2, CO_2, CO, CH_3OH and H_2O.

Species	Coverage
*	6.97E-01
CO*	3.70E-04
H2O*	2.99E-06
HCOOH*	1.24E-08
HCHO*	1.54E-12
H*	2.90E-01
OH*	3.15E-04
HCOO*	1.26E-02
H_2COOH*	2.91E-10
CH_3O*	8.80E-06
CH_3OH*	2.67E-07
CHO*	3.97E-12

Table S9. Reaction rate constant for reaction evolved in microkinetics simulation on Cu(211) at 500K

Reaction	k_+	k_-
CO+*→CO*	1.275E+10	1.042E+13
H_2O+*→H_2O*	1.031E+09	1.042E+13
CH_3OH+*→CH_3OH*	9.182E+07	1.042E+13
H_2+2*→H*+H*	5.525E+03	2.409E+03
OH*+H*→H_2O*+*	2.277E+05	2.296E+08
CO_2+H*→HCOO*	7.506E-03	1.080E+01
HCOO*+H*→HCOOH*+*	1.125E+02	1.087E+09
HCOOH*+H*→H_2COOH*+*	1.563E+06	2.830E+08
H_2COOH*+*→HCHO*+OH*	3.569E+08	2.554E+10
CO*+H*→CHO*+*	9.923E+03	8.856E+12
CHO*+H*→HCHO*+*	2.142E+08	1.788E+07
HCHO*+H*→CH3O*+*	7.091E+10	1.059E+05
CH3O*+H*→CH3OH*+*	1.882E+06	5.947E+08

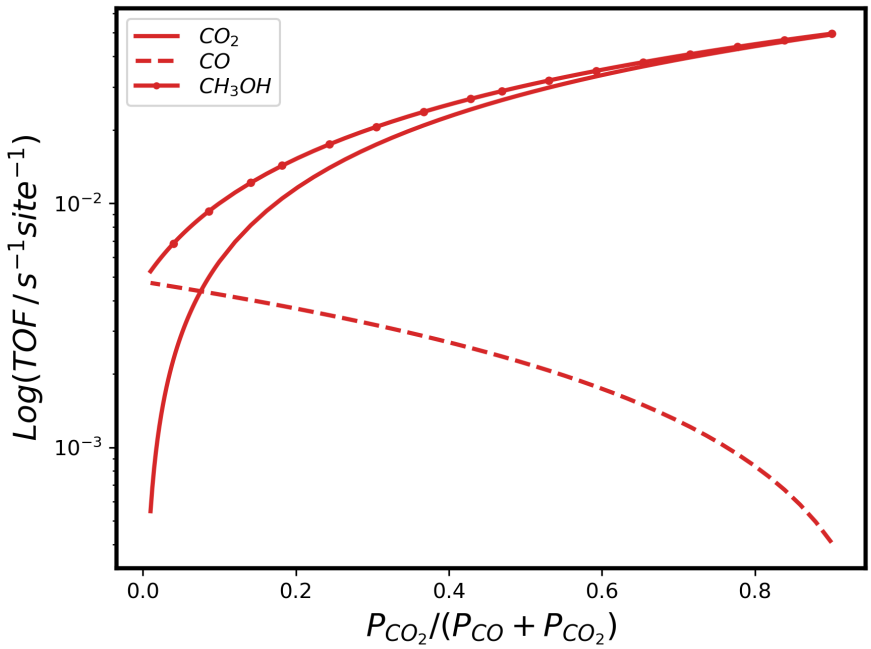

Figure S12. TOFs from microkinetics simulation of CO_2 and CO mixed gas hydrogenation as a function of CO2 content. Three lines are CO_2 consumption, CO consumption and methanol production TOF. Pressure is set as constant of 40, 1, 1 bar for H_2, CH_3OH, H_2O, respectively, and total pressure for CO_2 and CO is 20 bar.

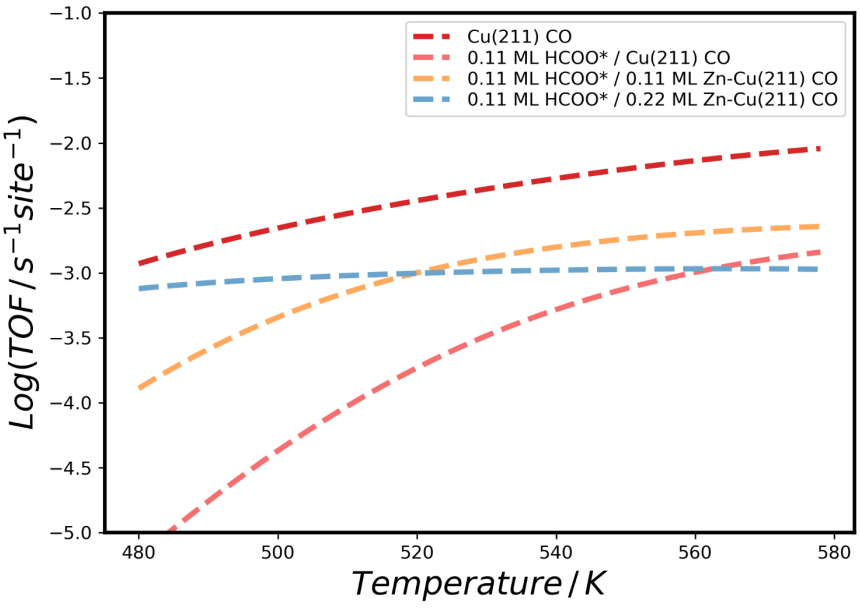

Figure S13 TOFs from microkinetics simulation for CO hydrogenation on 0.11 ML HCOO* / Cu(211) surface and its Zn surface alloy as a function of temperature. Pressure is set as constant of 10, 10, 40, 1, 1 bar for CO_2, CO, H_2, CH_3OH, H_2O, respectively.

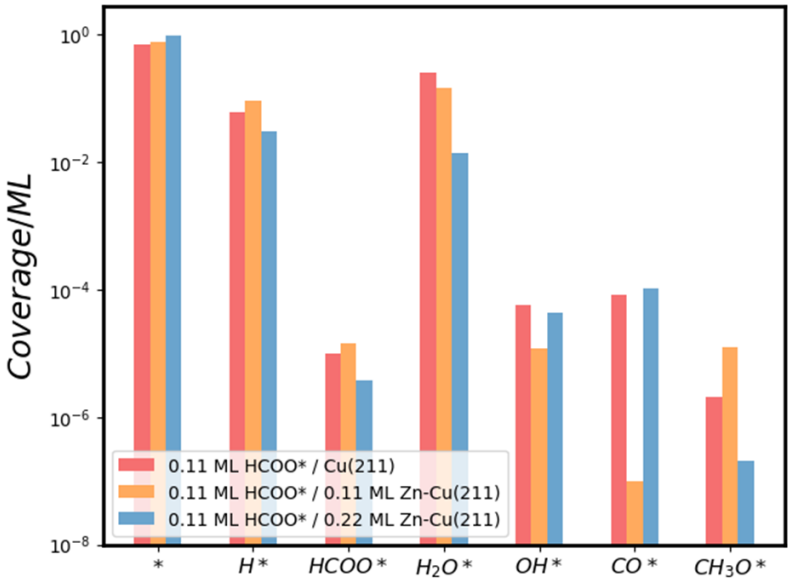

Figure S14 Surface coverage of main species on 0.11 ML HCOO* / Cu(211) surface and its Zn surface alloy

Reference:

(1) Zhang, X.-J.; Liu, Z.-P. Reaction Sampling and Reactivity Prediction Using the Stochastic Surface Walking Method. *Phys. Chem. Chem. Phys.* **2015**, *17* (4), 2757–2769. https://doi.org/10.1039/C4CP04456H.

(2) Zhang, X.-J.; Shang, C.; Liu, Z.-P. Stochastic Surface Walking Reaction Sampling for Resolving Heterogeneous Catalytic Reaction Network: A Revisit to the Mechanism of Water-Gas Shift Reaction on Cu. *The Journal of Chemical Physics* **2017**, *147* (15), 152706. https://doi.org/10.1063/1.4989540.

(3) Zhang, X.-J.; Shang, C.; Liu, Z.-P. Double-Ended Surface Walking Method for Pathway Building and Transition State Location of Complex Reactions. *J. Chem. Theory Comput.* **2013**, *9* (12), 5745–5753. https://doi.org/10.1021/ct4008475.

(4) Zhang, X.-J.; Liu, Z.-P. Variable-Cell Double-Ended Surface Walking Method for Fast Transition State Location of Solid Phase Transitions. *J. Chem. Theory Comput.* **2015**, *11* (10), 4885–4894. https://doi.org/10.1021/acs.jctc.5b00641.

(5) Rogers, D.; Hahn, M. Extended-Connectivity Fingerprints. *J. Chem. Inf. Model.* **2010**, *50* (5), 742–754. https://doi.org/10.1021/ci100050t.

(6) Kang, P.-L.; Shang, C.; Liu, Z.-P. Glucose to 5-Hydroxymethylfurfural: Origin of Site-Selectivity Resolved by Machine Learning Based Reaction Sampling. *J. Am. Chem. Soc.* **2019**, *141* (51), 20525–20536. https://doi.org/10.1021/jacs.9b11535.

(7) Chen, J.-F.; Mao, Y.; Wang, H.-F.; Hu, P. Reversibility Iteration Method for Understanding Reaction Networks and for Solving Microkinetics in Heterogeneous Catalysis. *ACS Catal.* **2016**, *6* (10), 7078–7087. https://doi.org/10.1021/acscatal.6b02405.

(8) Allison, T. C. NIST-JANAF Thermochemical Tables - SRD 13, 2013. https://doi.org/10.18434/T42S31.

(9) Burgess, D. R., Jr. Thermochemical Data. In *NIST Chemistry WebBook, NIST Standard Reference Database Number 69*; Linstrom, P. J., Mallard, W. G., Eds.; National Institute of Standards and Technology: Gaithersburg MD, 2021.

(10) Wang, V.; Xu, N.; Liu, J.-C.; Tang, G.; Geng, W.-T. VASPKIT: A User-Friendly Interface Facilitating High-Throughput Computing and Analysis Using VASP Code. *Computer Physics Communications* **2021**, *267*, 108033. https://doi.org/10.1016/j.cpc.2021.108033.

(11) Tameh, M. S.; Dearden, A. K.; Huang, C. Accuracy of Density Functional Theory for Predicting Kinetics of Methanol Synthesis from CO and CO_2 Hydrogenation on Copper. *J. Phys. Chem. C* **2018**, *122* (31), 17942–17953. https://doi.org/10.1021/acs.jpcc.8b06498.

(12) Behrens, M.; Studt, F.; Kasatkin, I.; Kuhl, S.; Havecker, M.; Abild-Pedersen, F.; Zander, S.; Girgsdies, F.; Kurr, P.; Kniep, B.-L.; Tovar, M.; Fischer, R. W.; Norskov, J. K.; Schlogl, R. The Active Site of Methanol Synthesis over Cu/ZnO/Al2O3 Industrial Catalysts. *Science* **2012**, *336* (6083), 893–897. https://doi.org/10.1126/science.1219831.

(13) Studt, F.; Abild-Pedersen, F.; Varley, J. B.; Nørskov, J. K. CO and CO2 Hydrogenation to Methanol Calculated Using the BEEF-VdW Functional. *Catal Lett* **2013**, *143* (1), 71–73. https://doi.org/10.1007/s10562-012-0947-5.

(14) Studt, F.; Behrens, M.; Kunkes, E. L.; Thomas, N.; Zander, S.; Tarasov, A.; Schumann, J.; Frei, E.; Varley, J. B.; Abild-Pedersen, F.; Nørskov, J. K.; Schlögl, R. The Mechanism of CO and CO_2 Hydrogenation to Methanol over Cu-Based Catalysts. *ChemCatChem* **2015**, *7* (7), 1105–1111. https://doi.org/10.1002/cctc.201500123.

(15) Wu, P.; Yang, B. Significance of Surface Formate Coverage on the Reaction Kinetics of Methanol Synthesis from CO2 Hydrogenation over Cu. *ACS Catal.* **2017**, *7* (10), 7187–7195. https://doi.org/10.1021/acscatal.7b01910.

(16) Vollmer, S.; Witte, G.; Wöll, C. Determination of Site Specific Adsorption Energies of CO on Copper. *Catalysis Letters* **2001**, *77* (1), 97–101. https://doi.org/10.1023/A:1012755616064.

(17) WS2-e. In *Thermochemical Data of Pure Substances*; John Wiley & Sons, Ltd, 1995; pp 1815–1885. https://doi.org/10.1002/9783527619825.ch12u.

(18) Behler, J.; Parrinello, M. Generalized Neural-Network Representation of High-Dimensional Potential-Energy Surfaces. *PHYSICAL REVIEW LETTERS* **2007**, 4.

(19) Huang, S.-D.; Shang, C.; Zhang, X.-J.; Liu, Z.-P. Material Discovery by Combining Stochastic Surface Walking Global Optimization with a Neural Network. *Chem. Sci.* **2017**, *8* (9), 6327–6337. https://doi.org/10.1039/C7SC01459G.

(20) Huang, S.-D.; Shang, C.; Kang, P.-L.; Liu, Z.-P. Atomic Structure of Boron Resolved Using Machine Learning and Global Sampling. *Chem. Sci.* **2018**, *9* (46), 8644–8655. https://doi.org/10.1039/C8SC03427C.

(21) Shang, C.; Huang, S.-D.; Liu, Z.-P. Massively Parallelization Strategy for Material Simulation Using High-Dimensional Neural Network Potential. *J. Comput. Chem.* **2019**, *40* (10), 1091–1096. https://doi.org/10.1002/jcc.25636.

(22) Huang, S.-D.; Shang, C.; Kang, P.-L.; Zhang, X.-J.; Liu, Z.-P. LASP: Fast Global Potential Energy Surface Exploration. *WIREs Comput. Mol. Sci.* **2019**, *9* (6), e1415. https://doi.org/10.1002/wcms.1415.

(23) Ma, S.; Shang, C.; Liu, Z.-P. Heterogeneous Catalysis from Structure to Activity via SSW-NN Method. *J. Chem. Phys.* **2019**, *151* (5), 050901. https://doi.org/10.1063/1.5113673.

(24) Martínez-Suárez, L.; Siemer, N.; Frenzel, J.; Marx, D. Reaction Network of Methanol Synthesis over Cu/ZnO Nanocatalysts. *ACS Catal.* **2015**, *5* (7), 4201–4218. https://doi.org/10.1021/acscatal.5b00442.

(25) Laio, A.; Gervasio, F. L. Metadynamics: A Method to Simulate Rare Events and Reconstruct the Free Energy

in Biophysics, Chemistry and Material Science. *Rep. Prog. Phys.* **2008**, *71* (12), 126601. https://doi.org/10.1088/0034-4885/71/12/126601.

(26) Grabow, L. C.; Mavrikakis, M. Mechanism of Methanol Synthesis on Cu through CO_2 and CO Hydrogenation. *ACS Catal.* **2011**, *1* (4), 365–384. https://doi.org/10.1021/cs200055d.

(27) Kattel, S.; Ramírez, P. J.; Chen, J. G.; Rodriguez, J. A.; Liu, P. Active Sites for CO_2 Hydrogenation to Methanol on Cu/ZnO Catalysts. *Science* **2017**, *355* (6331), 1296–1299. https://doi.org/10.1126/science.aal3573.

(28) Wang, S.-S.; Su, H.-Y.; Gu, X.-K.; Li, W.-X. Differentiating Intrinsic Reactivity of Copper, Copper–Zinc Alloy, and Copper/Zinc Oxide Interface for Methanol Steam Reforming by First-Principles Theory. *J. Phys. Chem. C* **2017**, *121* (39), 21553–21559. https://doi.org/10.1021/acs.jpcc.7b07703.

(29) Sun, X.; Wang, P.; Shao, Z.; Cao, X.; Hu, P. A First-Principles Microkinetic Study on the Hydrogenation of Carbon Dioxide over Cu(211) in the Presence of Water. *Sci. China Chem.* **2019**, *62* (12), 1686–1697. https://doi.org/10.1007/s11426-019-9639-0.

(30) Xu, D.; Wu, P.; Yang, B. Origin of CO_2 as the Main Carbon Source in Syngas-to-Methanol Process over Cu: Theoretical Evidence from a Combined DFT and Microkinetic Modeling Study. *Catal. Sci. Technol.* **2020**, *10* (10), 3346–3352. https://doi.org/10.1039/D0CY00602E.